Section 2

Data sets, diagnostic and dynamical investigations, statistical post-processing, reanalysis, and associated studies.

SPATIOTEMPORAL STRUCTURE OF THE FIRST- AND SECOND-ORDER TRENDS IN AIR TEMPERATURE IN THE 0-30-KM ATMOSPHERIC LAYER FOR THE NORTHERN AND SOUTHERN HEMISPHERES FROM RADIOSONDE DATA

I.V. Chernykh
Russian Institute of Hydrometeorological Information – World Data Center, Obninsk, Russia,
E-mail: civ@meteo.ru

Introduction

The information about the vertical structure of trends in air temperature in the atmosphere obtained from observations is necessary to study climate change. The paper presents the series of the first- and second-order trends [1] in air temperature (T) at standard heights in the 0–30- km atmospheric layer above sea level for different months, seasons and for the year as a whole for the Northern and Southern Hemispheres. The goal of this paper and of [1-4] is to show the longtime changes in the atmosphere for one period of radiosonde observations for the main aerological values. Calculations were made by Dr. O.A. Aldukhov.

Data and methods

Results of observations from the CARDS global aerological dataset [5] that were updated with the current data [6] for the period 1964–2018 were used in this study. The required condition for the station to be included into this study was the availability of 15-year observations from the full observation period including 2018. The Akima cubic spline interpolation method was used to calculate T values in the 0–30-km layer above sea level on the basis of standard pressure levels and specific points of vertical profiles. The linear trends were estimated for each station by using least squares method. The anomalies were computed with respect to the appropriate long-term mean values for the period of 1964–2018. The statistics obtained for all stations were averaged taking into account the area of the station influence.

Results

The Table presents ranges of intra-annual variations in monthly means for T and the first- and second-order trends in their anomalies in the 0–30-km atmospheric layer over the Northern and Southern Hemispheres, as well as, the months in which corresponding maximum/ minimum values were determined and the heights at which these values were determined. The corresponding maximum and minimum values were determined with significance of more than 95%.

Table. Ranges (Δ) of intra-annual variations of monthly averaged values for T *(C°),* and the first- (*C° per decade)* and second-order (*C° per decade*^{2}) decadal trends in their anomalies in the 0–30- km atmospheric layer over the Northern and Southern Hemispheres for the period 1964–2018. N is the number of soundings. The numerator shows in brackets the month (mm) in which maximum/ minimum values were determined. The height (h) at which maximum/ minimum values were determined is given in the denominator.

Δ mean, *C°* (mm)/ h	Δ first-order trends, *C° per decade* (mm)/ h	Δ second-order trends, *C° per decade*^{2} (mm)/ h	N, *millions*
Northern Hemisphere			
-67.17 (12) – 20.98 (08) 17 км 00 км	-0.375 (06) – 0.202 (04) 20 км 1 км	-0.060 (06) – 0.223 (05) 25 км 10 км	20,7
Southern Hemisphere			
-68.79 (07) – 18.47 (02) 17 км 00 км	-0.526 (11) – 0.164 (09) 18 км 2 км	-0.057 (02) – 0.159 (12) 25 км 15 км	3,2

The Figure shows a vertical macrostructure of long-term means, the first- and second-order trends in anomalies in temperature in the atmospheric layer under study for different months, seasons and the whole year for the Northern and Southern Hemispheres. Table and Figure reveal that the vertical structures of the first- and second-order linear trends in air temperature anomalies are not uniform in time and space. The study founded that there were some differences in the Northern and the Southern hemispheres. The main of them are listed below. The minimum value of the first-order trends (-0.526

Cº per decade) was detected at 18 km for Southern hemisphere in November, while the maximum value (0.202 Cº per decade) was found at 1 km over the Northern hemisphere in April. An amplitude of intra-annual changes of first-order trends in anomalies of monthly averaged values for T in the 0–30-km layer for the Northern hemisphere (0.577 Cº per decade) is smaller than that for the Southern hemisphere (0.690 Cº per decade). At the same time an amplitude of intra-annual changes of second-order trends in anomalies of monthly averaged values for T in the 0–30-km layer for the Northern hemisphere (0.283 Cº per decade^2) is larger than that for the Southern hemisphere (0.216 Cº per decade^2).

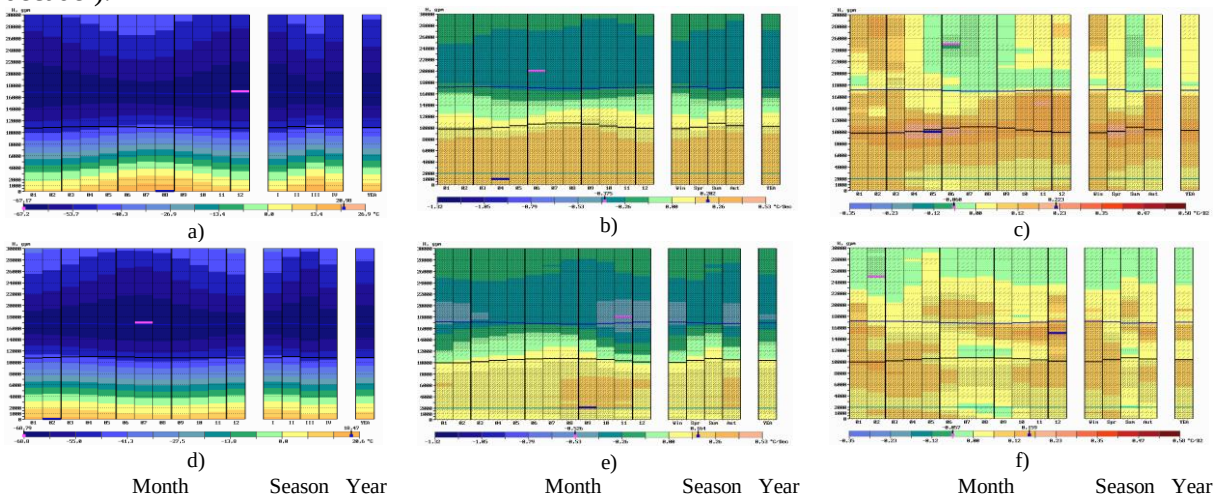

Figure. Long-term means (a, d, Cº), first-order trends in anomalies of long-term means for T (b, e, Cº per decade), second-order trends in anomalies of long-term means for T (c, f, Cº per decade^2) in the 0–30-km layer for the year as a whole, for each month and season. (a–c) – for the Northern and (d–f) – for the Southern hemispheres. Winter – DJF, spring – MMA, summer – JJA, autumn – SON. Blue and pink segments correspond to maximum and minimum values. The statistics for months and seasons were subject to twofold smoothing. The three–points smoothing was used. Trends with significance of not less than 50% are marked by the sloping line segments and those with significance of not less than 95% – by lattice. 1964–2018.

Conclusions

The computations are based on global aerological datasets for the period of 1964–2018. The following was found for both hemispheres. The vertical macrostructures of the first-order and second-order linear trends in air temperature anomalies are not uniform in the 0–30 km atmospheric layer above sea. Warming at 0–8 km and cooling at 16–30 km were detected for all months. With approaching to 2018 the highest acceleration in T changes was detected at 5-17 km in winter (DJF), at 0-1 km and at 4-13 km in spring (MMA), at 7-9 km and at 14-16 km in autumn (SON) and at 6-10 km and at 14-16 km for the year as a whole. The corresponding trends were detected with significance of more than 95%.

References

1. Aldukhov O.A., Chernykh I.V. First and second-order trends of air temperature at the surface level from global radiosonde data // Research activities in Earth system modelling. Working Group on Numerical Experimentation. Report No. 50. WCRP Report No.12/2020. Ed. E. Astakhova, July 2020, WMO, Geneva. http://bluebook.meteoinfo.ru/, 2020, p. 2-03-2-04
2. Aldukhov O.A., Chernykh I.V. Spatiotemporal distributions of global trends of water vapour amount in the 0-30 km atmospheric layer // Research activities in Earth system modelling. Working Group on Numerical Experimentation. Report No. 51. WCRP Report No. 4/2021. Ed.E.Astakhova, July 2021, WMO, Geneva. http://bluebook.meteoinfo.ru/, 2021. p. 2-03-2-04.
3. Aldukhov O.A., Chernykh I.V. Vertical macrostructure of first- and second- order trends of air temperature in the 0-30-km atmospheric layer from radiosonde observations // Research activities in Earth system modelling Working Group on Numerical Experimentation. Report No. 52. WCRP Report No. 4/2022. Ed.E.Astakhova, July 2022, WMO, Geneva. P. 2-03-2-04, http://bluebook.meteoinfo.ru/, 2022, p. 2-03-2-04
4. Chernykh I.V., Aldukhov O.A. Vertical Distribution of Trends of Relative Humidity in the 0-30-km Atmospheric Layer over the Northern and Southern Hemispheres from Radiosounding Data // Research activities in Earth system modelling. Working Group on Numerical Experimentation. Report No. 52. WCRP Report No. 4/2022. Ed. E. Astakhova, July 2022, WMO, Geneva. P. 2-07-2-08,http://bluebook.meteoinfo.ru/, 2022, p. 2-07-2-08
5. Eskridge R.E., et. al. A comprehensive aerological reference dataset (CARDS): rough and systematic errors // Bull. Amer. Meteor. Soc. 1995. **76.** 1759-1775.
6. Rudenkova T.V. Format for archiving of the current aerological data, received from GTS for PC // Proc. RIHMI-WDC, 2010, N 174, p. 41–63.

Deep convection and intense precipitation detection using geostationary weather satellite data: a case study of air-mass and concealed frontal convection

Gorlach I.A., Shishov A.E.[1]

Remote sensing methods for deep convection and intense precipitation detection are becoming more accessible for operative analysis and comparison with other meteorological methods. New technologies, software tools, visualisation systems, and composite products are developed to identify patterns within cloud systems and severe weather phenomena.

This paper is dedicated to the comparative analysis of satellite imagery and radar data based on the Deep Convection Cloud Monitoring System (DCCMS), developed by the authors [2]. The system provides a possibility to automatically detect deep convection and high rainfall rate (greater or less than 0.4 mm/h) zones based on brightness temperature and radar reflectivity measurements using a blend of thresholding and machine learning algorithms. It also provides interactive visualisation tools that are useful for further analysis. This paper describes the results of using DCCMS to study two cases of deep convection over European Russia (Figure 1): air-mass convection (7 July 2022) and concealed frontal convection (2 October 2022).

Rainfall rate (mm/h) was estimated based on 10-minute radar reflectivity (maximum value over 11 vertical levels) from radar network DMRL-S over European Russia to serve as the ground truth for both the air-mass deep convection case (7 July 2022) and the frontal clouds with concealed convection case (2 October 2022). Spatial resolution of these measurements was equal to 1x1 km.

Brightness temperature measurements in the infrared window (with the central wavelength equal to 10.8 micrometres) derived from meteorological geostationary satellite Meteosat-10 images were used to calculate rainfall rate according to a formula proposed in [1]. Temporal and spatial resolutions of these observations were equal to 5 min and 5x5 km, respectively.

The application of the DCCMS system designed for automated deep convection detection using machine learning algorithms allowed to identify deep convection regions (masks) in satellite images (Figure 1b) and evaluate high rainfall rate conditions in air-mass and concealed frontal deep convection (Figure 2).

The datasets were reprojected and resampled to match in space and time. Overall, 144 time periods of scene observations (images) were selected for each of the considered cases.

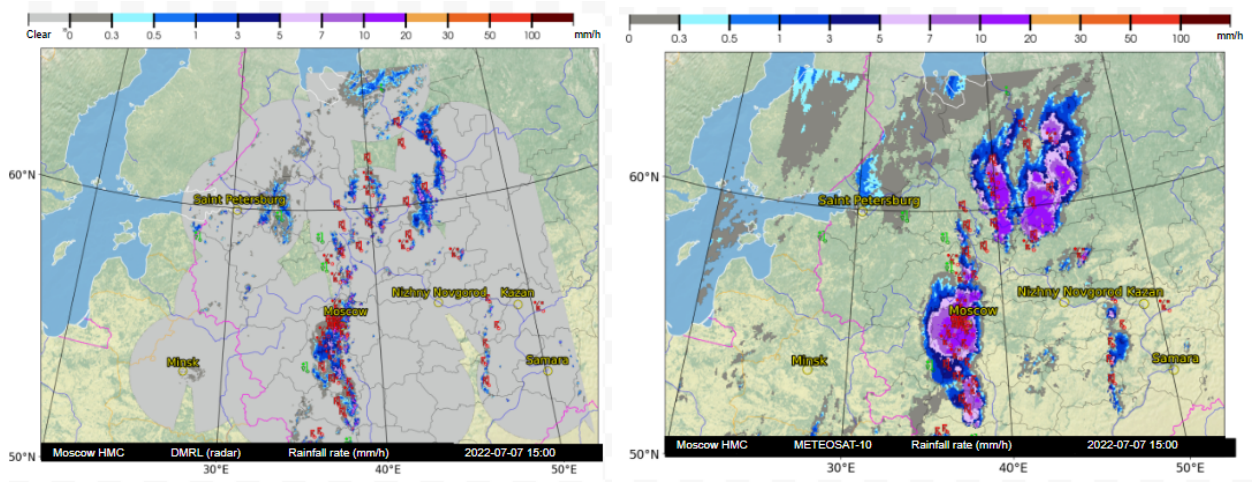

a) **b)**

Fig.1 Rainfall rate (mm/h) distribution estimated from radar (a) and satellite (b) data for 2022-07-07

[1] The Hydrometcentre of Russia, 123242 Moscow, Russia, B. Predtechenskiy per., shandruha@gmail.com

The comparison method consisted in pixel grouping according to the rainfall rate values derived from DMRL data: greater than 4 mm/h - showers present (SP), less than 4 mm/h - showers not present (SN). The following detection accuracy metrics have been computed: probability of detection (%) for phenomena from "SP" group - POD_{SP}; probability of detection (%) for phenomena from "SN" group - POD_{SN}; false alarm rate (%) - FAR. Hourly radar and satellite remote sensing data comparison results are depicted in Figure 2a) and 2b).

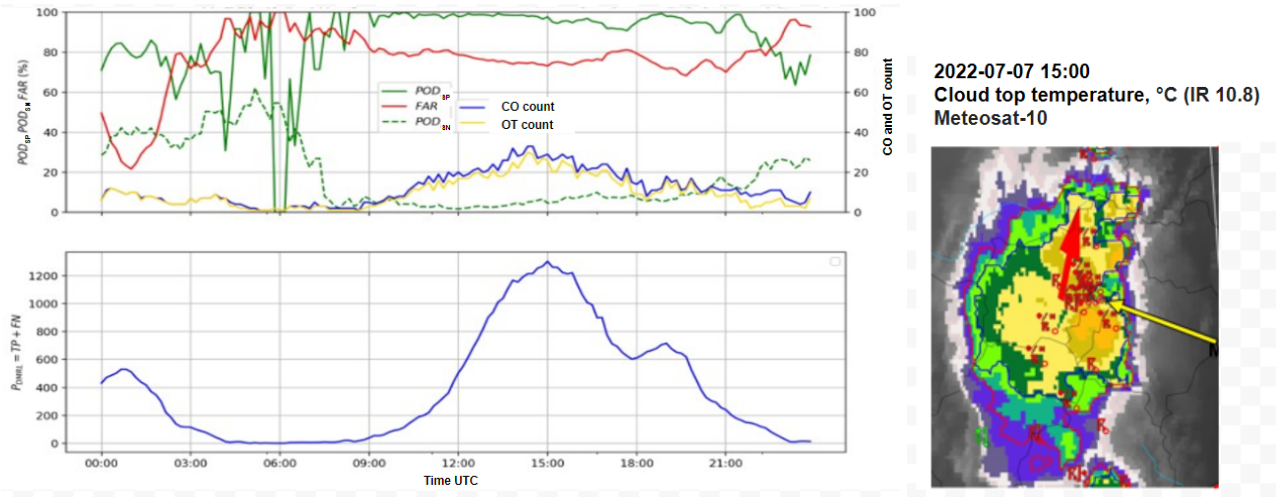

a)

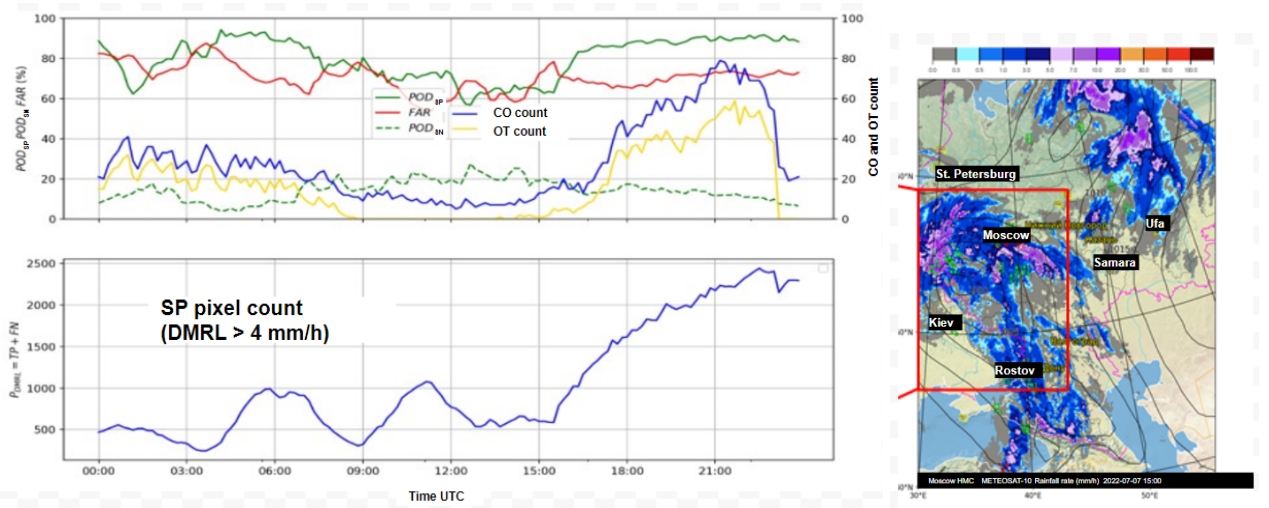

b)

Fig. 2. Rainfall rate estimates (greater and less than 4 mm/h) comparison within and outside deep convection clouds for 2022-07-07 (a) and 2022-10-02 (b)

In conclusion, the detection of high rainfall rate regions proved to be accurate within deep convection zones (with POD varying from 90 to 100%), but the presence of false alarms, particularly in the case of small isolated cores, indicates the need for further improvement of the proposed algorithms.

References

1. Vicente G. A., Scofield R.A., Menzel W.P. The Operational GOES Infrared Rainfall Estimation Technique // Bulletin of the American Meteorological Society. – 1998. – T. 79. – № 9. – C. 1883-1898.

2. Shishov A.E., Gorlach I.A. Computer Software Copyright Registration Certificate No. 2022680485 from 01.11.2022. - Deep convection cloud monitoring system (DCCMS). «Hydrometcentre of Russia».2022.01.11.

Statistical Bias Correction of NCMRWF Unified Model Precipitation Forecasts Based on Quantile Mapping Methods

Kondapalli Niranjan Kumar, Sukhwinder Kaur, Shubha Singh, Mohana Satyanarayana Thota, Raghavendra Ashrit, Ashis K. Mitra & V S Prasad

National Centre for Medium Range Weather Forecasting, Ministry of Earth Sciences, Noida,

India Email: niranjan.kondapalli@gov.in

1. Introduction

The model forecasts frequently show systemic errors in relation to the observations and, more significantly, in relation to the crucial variables, like precipitation. Thus, it is essential to correct the model errors to efficiently utilize NWP forecasts for decision-making applications for flood risk management. In this study, we particularly focused on the assessment of location-specific bias correction methods for Mumbai (BOM, 72.85^{o}E, 19.117^{o}N), located on India's western coast. This location is chosen here to support the Integrated Flood Warning System (IFLOWS), initiated by the Ministry of Earth Sciences, Government of India, which provides early warning and decision support during flooding. Mumbai city experiences strong westerly and southwesterly flow because of summer monsoon winds from the Arabian Sea because of its geographic location on the windward side of the Western Ghats of India. This causes orographic rainfall with a high magnitude and intensity. In addition, the city is also affected by other significant weather features including offshore vortices and troughs, depressions in the Arabian Sea, and most significantly, mid-tropospheric cyclones (MTCs), which bring hazardous rainfall during the southwest monsoon. The novelty and significance of this work lie in using a newly developed high-resolution Indian Monsoon Data Assimilation and Analysis (IMDAA, Rani et al., 2012) reanalysis product in calibrating the National Centre for Medium Range Weather Forecasts (NCMRWF) Unified Model (NCUM) operational forecasts (Sumit Kumar et al., 2021) for improving rainfall forecasts at a local scale. The NWP dynamical cores used to generate the IMDAA reanalysis data and the NCUM daily operational forecasts are quite similar. Hence, as they employ the same model physics, IMDAA can be efficiently used to correct real-time forecasts. It is also important to note that the calibration methods adjust the model's systematic biases which are equivalent to many years of improvement to the basic model.

2. Methodology

Statistical bias correction techniques establish a link/relationship between observed and simulated variables over the historical period and then utilize the functional relationship to bias-correct the model predictions. In this study, we used empirical quantile mapping (EQM), parametric quantile mapping (PQM), and gamma/generalized Pareto parametric quantile mapping (GPQM) techniques (Niranjan Kumar et al., 2021). EQM is a non-parametric bias correction method that calculates quantile-by-quantile modifications/changes in the simulated cumulative distribution function to correct the mean and variability, including shape errors. However, PQM and GPQM are parametric bias correction techniques. The PQM technique assumes that both observed and simulated intensities are well approximated with two-parameter gamma distributions and uses a theoretical distribution rather than an empirical distribution. While the GPQM method is based on gamma distribution combined with generalized Pareto distribution (GPD).

3. Quantile Mapping Bias Correction

Figure 1 (left panel) shows the time evolution of India Meteorological Department (IMD) station rainfall (OBS), NCUM Day-1 raw forecasts (FCS), and bias-corrected Day-1 rainfall forecasts based on EQM (FCS_{eqm}), PQM (FCS_{pqm}), and GPQM (FCS_{gpqm}) methods. The observed rainfall over BOM indicates heavy to very heavy rainfall events (>64.5mm/day) defined by IMD during the southwest monsoon season (JJAS 2022). Figure 1 (right panel) indicates skill scores based on raw and bias-

corrected forecasts. Figure 1 (right panel) depicts the HIR (Hit rate), and ETS (Equitable threat score) scores for bias-corrected forecasts that have higher magnitudes for rainfall events with magnitudes more than 100mm/day along with low False alarm rate (FAR). Hence, the heavy to very heavy rainfall events are better calibrated based on the parametric methods which will be useful for early warning and decision support for flooding during extreme rainfall events over the Mumbai city. The results from our study indicate that the GPQM performance is relatively better while correcting the raw forecasts, especially, during heavy rainfall cases.

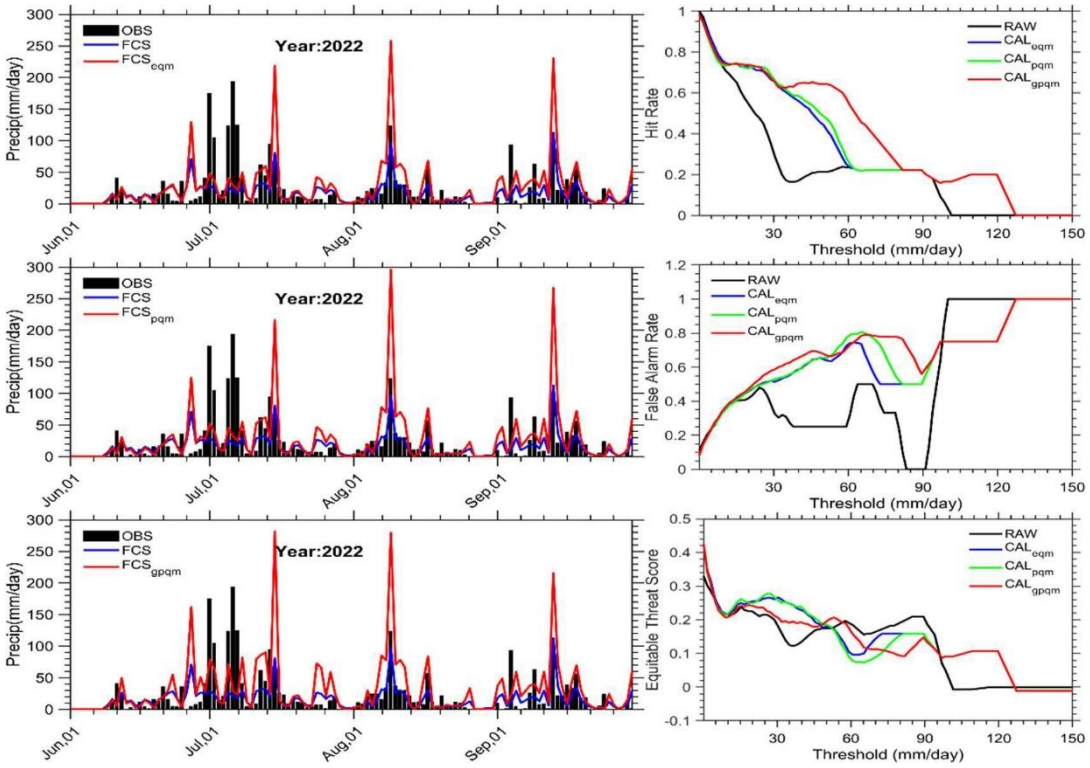

Figure 1 (left panel) Time evolution of observed and model forecast rainfall along with calibrated rainfall based on quantile mapping bias-correction methods for the period between Jun-Sep, 2022. (Right panel) Model skill scores such as Hit Rate (HIR), False Alarm Rate (FAR), and Equitable Threat Score (ETS) are estimated based on IMD station rainfall vs raw and bias-corrected model forecasts.

4. References

[1]. Niranjan Kumar et al., (2022) Quantile mapping bias correction methods to IMDAA reanalysis for calibrating NCMRWF unified model operational forecasts, Hydrological Sciences Journal, 67:6, 870-885, DOI: https://doi.org/10.1080/02626667.2022.2049272

[2]. Rani, S.I., et al., 2021. IMDAA: high resolution satellite-era reanalysis for the Indian monsoon region. Journal of Climate, 1–78. doi:10.1175/JCLI-D-20- 0412.1

[3]. Sumit Kumar et al., (2021), NCUM Global DA System: Highlights of the 2021 upgrade, NCMRWF Technical Report No. NMRF/TR/05/2021, https://www.ncmrwf.gov.in/Reports- php/Highlights_upgrade_report.php

Tropical cyclone activity in the Bay of Bengal during ENSO-IOD events

Biranchi Kumar Mahala[1]*, Birendra Kumar Nayak[2], Pratap Kumar Mohanty[3]

[1]School of Applied Sciences (Mathematics), Kalinga Institute of Industrial Technology (KIIT), Deemed to be University, Bhubaneswar, Odisha, India
[2] Department of Mathematics, Utkal University, Vani Vihar, Bhubaneswar 751004, Odisha, India
[3] Department of Marine Sciences, Berhampur University, Berhampur, Odisha, India

E-mail: *biranchimahala@gmail.com, bknatuu@yahoo.co.uk, pratap_mohanty@yahoo.com,

1. Introduction:

The North Indian Ocean (NIO) is one of the important basins contributing about 7% of total tropical cyclones (TCs) over the world. El-Niño-Southern Oscillation (ENSO) a genuine ocean-atmospheric phenomenon born out of active interaction between the two components of the climate system and is considered as the most dominant inter-annual mode of tropical coupled ocean-atmosphere system (McPhaden 2002). ENSO events last approximately 12-18 months and occur every two to seven years with large variation in strengths (Chang et al. 2006). The co-occurrence of ENSO and Indian Ocean Dipole (IOD) events make it difficult to reach a clear conclusion of complex IOD-ENSO interaction on TC activity in the Bay of Bengal (BoB). In the present study, we use long term tropical cyclone climatology (1891-2007) to study the impacts of ENSO and IOD on intensity, frequency, genesis location, average lifetime of TC in BoB.

2. Data and Methodology:

The domain for the present study covers the entire BoB region. Niño3.4 and Oceanic Niño Index (ONI) values were employed for the period 1891-1949 and 1950-2007 respectively to determine the El Niño, La Niña and neutral ENSO years for the study period1891-2007. Dipole Mode Index (DMI) was used to classify the years as +ve IOD, –ve IOD and no IOD. In the present study, TC includes Cyclonic storms (CS (with maximum sustained wind (MSW) 34–47 knots) and Severe cyclonic storms (SCS) (with MSW ≥48 knots). An El Niño (La Niña) year is identified if the 5-month running-average of the Niño3.4 Index exceeds +0.4°C (-0.4°C) for at least 6 consecutive months. When the DMI is positive then, the phenomenon is referred as the +ve IOD and when it is negative, it is referred as –ve IOD. In this study we have computed the mean of the DMI from June-November of every year and assigned the value to represent the DMI of that particular year.

3. Results and Discussion:

Out of 502 TCs over BoB during 117-year study period (1891–2007), 178,169 and 155 TCs were observed during El Niño, neutral ENSO and La Niña years. The average frequency of TC per year during El Niño, neutral ENSO and La Niña years are computed as 4.23, 4.02 and 4.69 respectively. In this study, 33 years were identified as La Niña years while El Niño and neutral ENSO years were 42 each. Out of the 117 years of study period, number of +ve IOD, –ve IOD and no IOD years were identified as 18, 17 and 82 respectively. As a means to investigate the most probable period for TC formation in the BoB, the TC season from first one third of April to December 31 was divided into 10-day or one-third monthly intervals for the 117 years study period. Table 1 shows the TC season divided into 10-day intervals, the total number of TC formations, and the average number of TC that occurred for the 10-day intervals during the 117-year period of study. A close inspection of the data in the Table 1 for the months of April through December shows maximum peaks in TC development (primary TC peak period) during first third of November and is considered as the most favoured period of TC formation followed by during second one third of November and last one third of October. Genesis location decides the track length which plays an important role on life time and intensity of TC (Camargo et al. 2007). Therefore, to get detailed information on the genesis location and its consequent role on TC cycle, we divided the BoB into four quadrants; R_1 (15-26ºN, 88.3º-100ºE), R_2 (15-26ºN, 76.3-88.3ºE), R_3 (5-15ºN,76.3-88.3ºE) and R_4 (5-15ºN, 88.3-100ºE) and computed the TCs formed in each quadrant (Fig. 1) for different ENSO and IOD years. During El Niño years total no of TCs formed are more than those during La Niña and neutral ENSO years. During El Niño years maximum (minimum) number of TCs are formed in R_3 (R_2) while during La Niña and neutral ENSO years, maximum (minimum) numbers of TCs are formed in R_4 (R_2). During +ve IOD, –ve IOD and no IOD years maximum (minimum) TCs are formed in R_4 (R_2). Comparison of frequency of formation of TCs in a particular quadrant under different IOD conditions reveals that maximum TCs are formed in R_1, R_2 during –ve IOD years and in R_3, R_4 during +ve IOD years. Life time of TCs has important implications on the intensity of TC and damage. During El Niño years, average life time of TCs is relatively shorter as compared to those during La Niña and neutral ENSO years (Table 2). The results corroborate with our observation made earlier regarding the genesis location of TCs; i.e. during El Niño years, TCs mostly form in R_3 followed by R_1 and hence have shorter life time than the TCs in R_4 during La Niña and neutral ENSO years which are away from the coast. The results also agree with the observations of Girishkumar and Ravichandran (2012), albeit with a longer life time. Further, it is observed that TCs formed over R_4 have longer life time followed by over R_1 during El Niño years while during La Niña and neutral ENSO years; TCs formed over R_1 have longer life time followed by over R_2. Life time of TCs formed over R_3 is however shorter in all types of ENSO events. Average life time of TCs is relatively longer (shorter) during +ve (–ve and no IOD) IOD years. The study shows that, TCs formed over R_1 have longer life time in all types of IOD events.

4. References:

Camargo, S. J., Robertson, A. W., Gaffney, S. J., Smyth, P., & Ghil, M. (2007). Cluster analysis of typhoon tracks. Part I: General properties. *Journal of Climate*, *20*(14), 3635-3653.

Chang, P., Yamagata, T., Schopf, P., Behera, S. K., Carton, J., Kessler, W. S., ... & Xie, S. P. (2006). Climate fluctuations of tropical coupled systems—the role of ocean dynamics. *Journal of Climate*, *19*(20), 5122-5174.
Girishkumar, M. S., & Ravichandran, M. (2012). The influences of ENSO on tropical cyclone activity in the Bay of Bengal during October–December. Journal of Geophysical Research: Oceans, 117(C2).
McPhaden, M. J. (2004). Evolution of the 2002/03 El Niño. Bulletin of the American Meteorological Society, 85(5), 677-696.

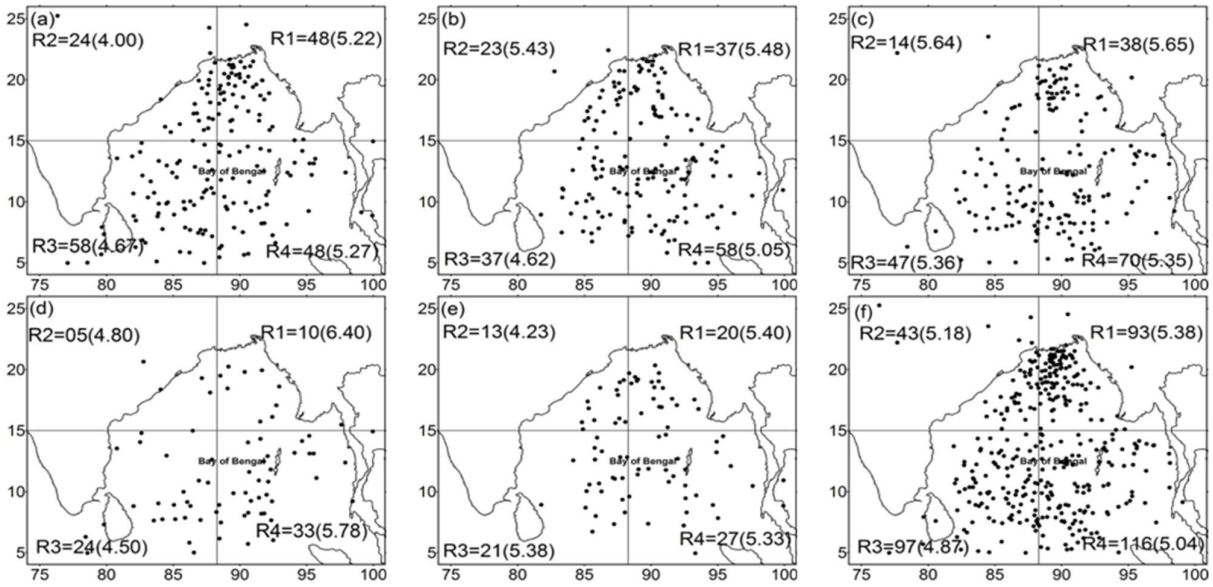

Fig 1 Genesis location of TCs during the ENSO/IOD events during 1891-2007 (a) El Niño years, (b) La Niña years, (c) Neutral ENSO years, (d) +ve IOD years, (e) –ve IOD years, (f) No IOD years.

Table 1 TCs formed over BoB during 1891-2007 for one-third monthly intervals

MONTH	Date ($1/3^{rd}$ of a month)	TOTAL	Average per year
APRIL	1-10	2	0.017
APRIL	11-20	6	0.051
APRIL	21-30	16	0.136
MAY	1-10	18	0.153
MAY	11-20	20	0.170
MAY	21-31	17	0.145
JUNE	1-10	14	0.119
JUNE	11-20	10	0.085
JUNE	21-30	17	0.145
JULY	1-10	10	0.085
JULY	11-20	13	0.111
JULY	21-31	20	0.170
AUGUST	1-10	12	0.102
AUGUST	11-20	12	0.102
AUGUST	21-31	7	0.059
SEPTEMBER	1-10	8	0.068
SEPTEMBER	11-20	14	0.119
SEPTEMBER	21-30	22	0.188
OCTOBER	1-10	16	0.136
OCTOBER	11-20	32	0.273
OCTOBER	21-31	38	0.324
NOVEMBER	1-10	46	0.393
NOVEMBER	11-20	42	0.358
NOVEMBER	21-30	28	0.239
DECEMBER	1-10	19	0.162
DECEMBER	11-20	12	0.102
DECEMBER	21-31	16	0.136

Table 2 Life time (in days) of TCs during ENSO/IOD events

Event	El Niño	La Niña	Neutral ENSO	Positive IOD	Negative IOD	No IOD
Days	4.89	5.13	5.44	5.37	5.18	5.1

Large-scale features of active and break phases during Indian summer monsoon 2022

Sujata K. Mandke[1], *
[1]Indian Institute of Tropical Meteorology, Ministry of Earth Sciences, India
*amin@tropmet.res.in

1. Introduction

A substantial component of the Indian summer Monson (ISM) rainfall variability arises from the fluctuation on subseasonal scale between active and break spells. The subseasonal variation of monsoon rains over India have a strong bearing on the rainfed agriculture. Despite significant progress in understanding intraseasonal variability of ISM (Goswami, 2005), there is lack of understanding of the complex processes leading to active-break phases. The convection and circulation patterns fluctuate between active-break events, which are part of the large-scale shifts associated with monsoon intraseasonal oscillations (Annamalai and Slingo, 20001). The present study diagnoses the large-scale changes in the convection and circulation during active-break periods of contrasting rainfall conditions during ISM 2022, that are identified based on the criteria by India Meteorological Department as the periods in which the normalized anomaly of the rainfall averaged over the core monsoon zone (CMZ) (18- 28°N, 65°E-88°E) exceeds 1 or is less than −1.0 respectively, provided the criterion is satisfied for at least three consecutive days.

2. Data

Datasets used are: (a) Global Precipitation Climatology Project (GPCP) daily precipitation (mm) (1°x1°) (b) Daily wind (m/s), Geopotential height (GPH) (m) and vertical velocity (omega) (pascal/second) (2.5°×2.5°) at different vertical levels from National Center for Environmental Prediction/National Centre for Atmospheric Research (NCEP/NCAR) Reanalysis.

3. Results

To isolate the large-scale spatial structure of rainfall and circulation changes between an active (9-15th July 2022) and break (26th August – 3rd September 2022) spell, spatial plot of precipitation anomaly, wind anomaly at 850hPa, GPH at 200hPa, divergence anomaly at 200hPa and latitude-pressure section of vertical velocity (omega) averaged over the Indian longitudes (73°-82°E) depicting Hadley circulation is illustrated separately for active and break spell, along with the difference (active-break) spell in (Figure 1(a-o)) respectively. Precipitation anomalies features 'quadrupole' structure with enhanced (decreased) precipitation over central India, extending over the Bay of Bengal and equatorial west Pacific, while decreased (enhanced) precipitation over the south-eastern tropical Indian Ocean (SETIO) and northwest tropical Pacific during an active (break) phase (Figure 1(a, b)) (Annamalai and Slingo,2001). The low-level mean monsoon circulation, monsoon trough and the cross-equatorial jet over Somali is strengthened (weakened) in active (break) phase. The low-level anomalous anticyclonic circulation over head Bay of Bengal (BOB) caused reduced precipitation during break (Figure 1(d, e)).

In the upper troposphere, the local circulation associated with active phase is characterised by extended Tibetan anticyclone (TA) with two-cell structure of the core of TA (Basha et al. 2020). The extent of TA is less in break spell compared to active spell (Figure 1(g-i)). Intensified TA reinforced the strong horizontal divergence in the upper level (Figure 1j) initiating the outbreak of convection over India in an active phase. The upper-level divergence is enhanced over CMZ stretching south eastward to central and southeast BOB, Maritime continent, and equatorial west Pacific Ocean in active phase (Figure 1j), whereas it is enhanced over south peninsular India, southwest Arabian sea and SETIO during break phase (Figure 1k). Location and spatial pattern of strong positive upper-level divergence anomalies correspond well with those of increased precipitation anomalies. The intensified (weakened) lower and upper tropospheric flow over the monsoon domain corroborates that the large-scale Hadley circulation is substantially strengthened (weakened) during active (break) phase **(**Figure 1(m, n)). The enhanced low-level cyclonic (anticyclonic) circulation anomaly in the monsoon trough region during an active (break) condition (Figure 1 (d, e)) is associated with enhanced (decreased) ascending motion (Figure 1(m, n)), causing enhanced (decreased) precipitation over the monsoon trough region and decreased (enhanced) ascending motion and decreased (enhanced) precipitation over the equatorial warm waters (Figure 1(a,b)). Thus, regional Hadley circulation oscillates between northern position around the monsoon trough region and southern location over an equatorial ocean between an active (break) phase.

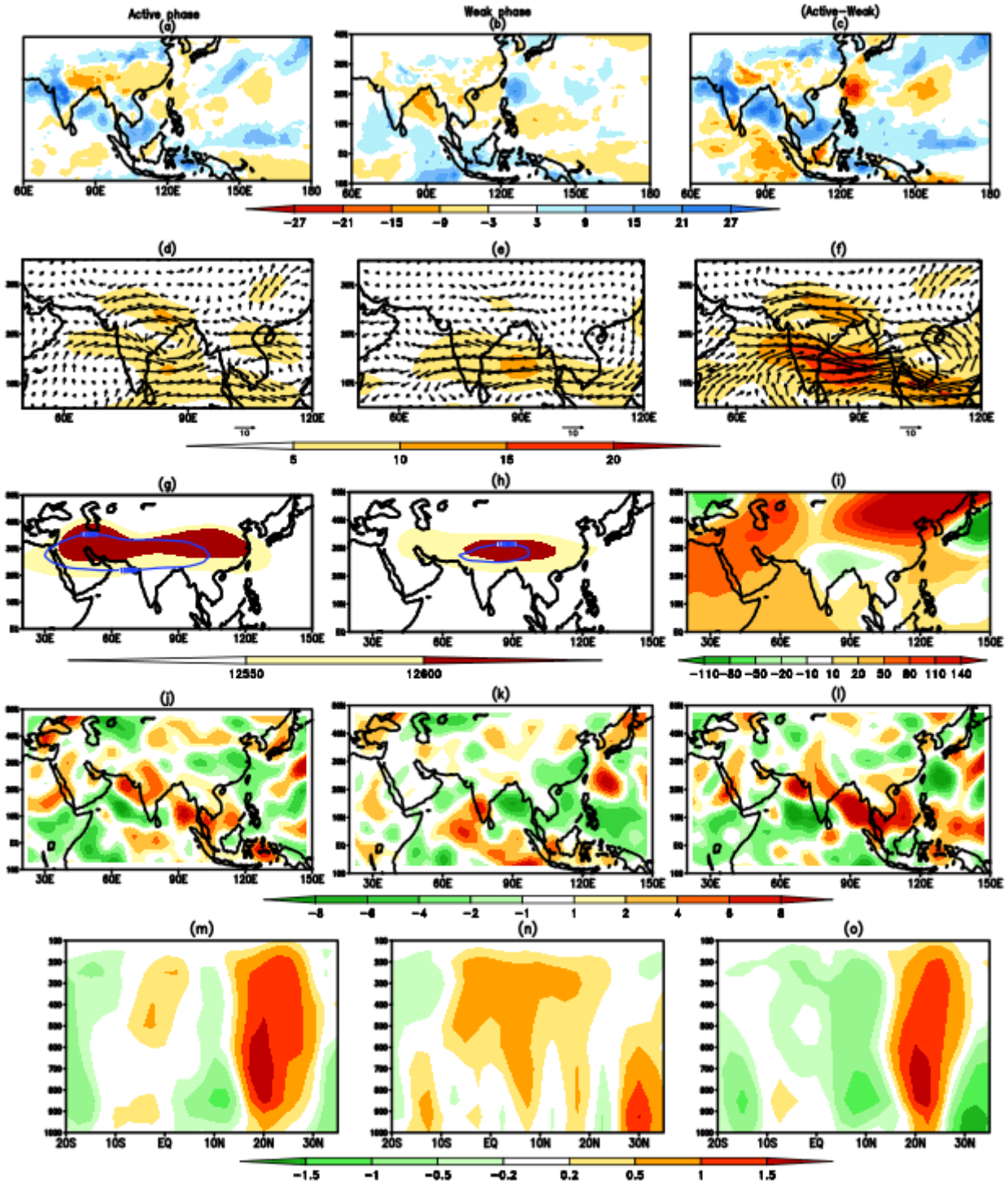

Figure 1. Spatial plot of precipitation anomaly for (a)Active spell (b)Break spell (c) Difference (Active-Break). (d, e, f) are same as (a, b, c) respectively, except wind anomaly at 850hPa. (g, h, i) are same as (a, b, c) respectively, except Geopotential height at 200hPa (shaded) overlaid by climatology (blue contour). (j, k, l) are same as (a, b, c) respectively except divergence anomaly at 200hPa (*10^6). (m, n, o) are latitude-pressure section of vertical velocity (omega*-10) averaged over Indian longitudes (73°-82°E) during Active spell, Break spell and difference (Active-Break) spell, respectively.

References: Annamalai H, Slingo JM. 2001. Active/break cycles: diagnosis of the intraseasonal variability of the Asian summer monsoon. Clim. Dyn. 18:85–102.

Basha, G., Venkat Ratnam, M., and Kishore, P. 2020. Asian summer monsoon anticyclone: trends and variability, Atmos. Chem. Phys., 20:6789–6801.

Goswami, B.N. 2005. In: William, K.M., Lau, Duane, E.Waliser (Eds.), South Asian Monsoon: in Intraseasonal Variability of the Atmosphere–Ocean Climate System. Praxis, Springer, Berlin Heidelberg, Chapter 2, 19–61.

The association of West Pacific subtropical high variability with the Indian summer monsoon 2022

Sujata K. Mandke [1, *]
[1]Indian Institute of Tropical Meteorology, Ministry of Earth Sciences, India
*amin@tropmet.res.in

1. Introduction

Apart from ENSO, the variability in the intensity and location of West Pacific Subtropical High (WPSH) is closely linked with the interannual and sub-seasonal rainfall variations over India (Chowdhary et al., 2013,2019; Huang et al., 2018; Chaluvedi et al., 2021). However, connection of WPSH with the daily variation of summer monsoon rainfall over India is still not examined. WPSH is an anticyclonic system in the lower troposphere over the northwestern Pacific, which is strongest during boreal summer. This study investigates the association between WPSH variability and daily summer monsoon rainfall variations during 25-30th June 2022.

2. Data

Datasets used are: (i) Global Precipitation Climatology Project (GPCP) daily precipitation (mm) (1°x1°) (b) Daily wind (m/sec), Mean sea-level pressure (MSLP; hPa), specific humidity (g/kg) on (2.5°×2.5°) at different vertical levels from National Centre for Environmental Prediction/National Centre for Atmospheric Research (NCEP/NCAR) Reanalysis (Kalnay et al., 1996).

3. Results

Daily precipitation anomaly over Indo-Pacific region during 25-30th June 2022 is illustrated in Figure 1(left column). MSLP overlaid by the climatology (Figure 1; 2nd column) and MSLP anomaly (Figure 1; 3rd column) over the Pacific Ocean for 25-30th June 2022 is illustrated. The centre of WPSH is shifted northward during 25-27th June 2022, while intensification and westward extension of western flank of WPSH is noted from 28-30th June 2022. Precipitation is enhanced over parts of west and central India (Chaluvedi et al.,2021), South China Sea extending to the Philippine Sea, whereas it is largely reduced over Bay of Bengal (BOB) (Chowdhary et al., 2013), coincident with the strong and westward expanded WPSH during 28-30th June 2022. On the contrary, northward shift of WPSH induced suppressed rainfall over most regions of India except eastern parts, during 25-27th June 2022. The large-scale circulation fluctuation owing to variation in WPSH results in the changes in moisture supply from the Arabian Sea, Bay of Bengal and west Pacific Ocean, thereby affecting large-scale precipitation (Chaluvedi, et al, 2021). Thus, to understand the link between WPSH and precipitation over India, vertically integrated (from the surface to 300 hPa) moisture transport overlaid by moisture flux convergence during 25-30th June 2022 is examined (Figure 1; 4th column). The supply of moisture from the southern flank of intense westward extended WPSH, besides strong cross equatorial flow across the Arabian Sea (figure not shown), lead to increased precipitation over west and central regions of India during 28-30th June 2022. On the other hand, changes in the large-scale circulation over Indo-Pacific region due to northward shift of WPSH may be unfavourable for precipitation over India from 25-27th June 2022, resulting in decreased precipitation over most parts of India. This analysis suggests the importance of the Western Pacific circulation associated with WPSH variability in daily rainfall variations over India.

References:

Gnanaseelan, C., Chowdary, J.S. 2019. The Indo-Western Pacific climate variability and impacts on Indian summer monsoon: two decades of advancement in India. Mausam, 70, 4:731-752.

Chaluvadi R, Varikoden H, et.al., 2021. Variability of West Pacific subtropical high and its potential importance to the Indian summer monsoon rainfall. Int. J. Climatology, 41:4047–4060.

Chowdary, J.S., Gnanaseelan, C. and Chakravorty, S. 2013. Impact of Northwest Pacific anticyclone on the Indian summer monsoon region. Theor. and Appl. Climatology, 113:329–336.

Chowdary, J.S., Srinivas, G. et al., 2019. Month-to-month variability of Indian summer monsoon rainfall in 2016: role of the Indo-Pacific climatic conditions. Climate Dynamics, 52:1157–1171

Kalnay, E., et al., 1996. The NCEP/NCAR 40-year re-analysis project. Bull. Amer. Met. Soc. 77: 437–471.
Huang, Y., Wang, B., et al., 2018. Changes in the influence of the western Pacific subtropical high on Asian summer monsoon rainfall in the late 1990s. Climate Dynamics, 51:443–455.

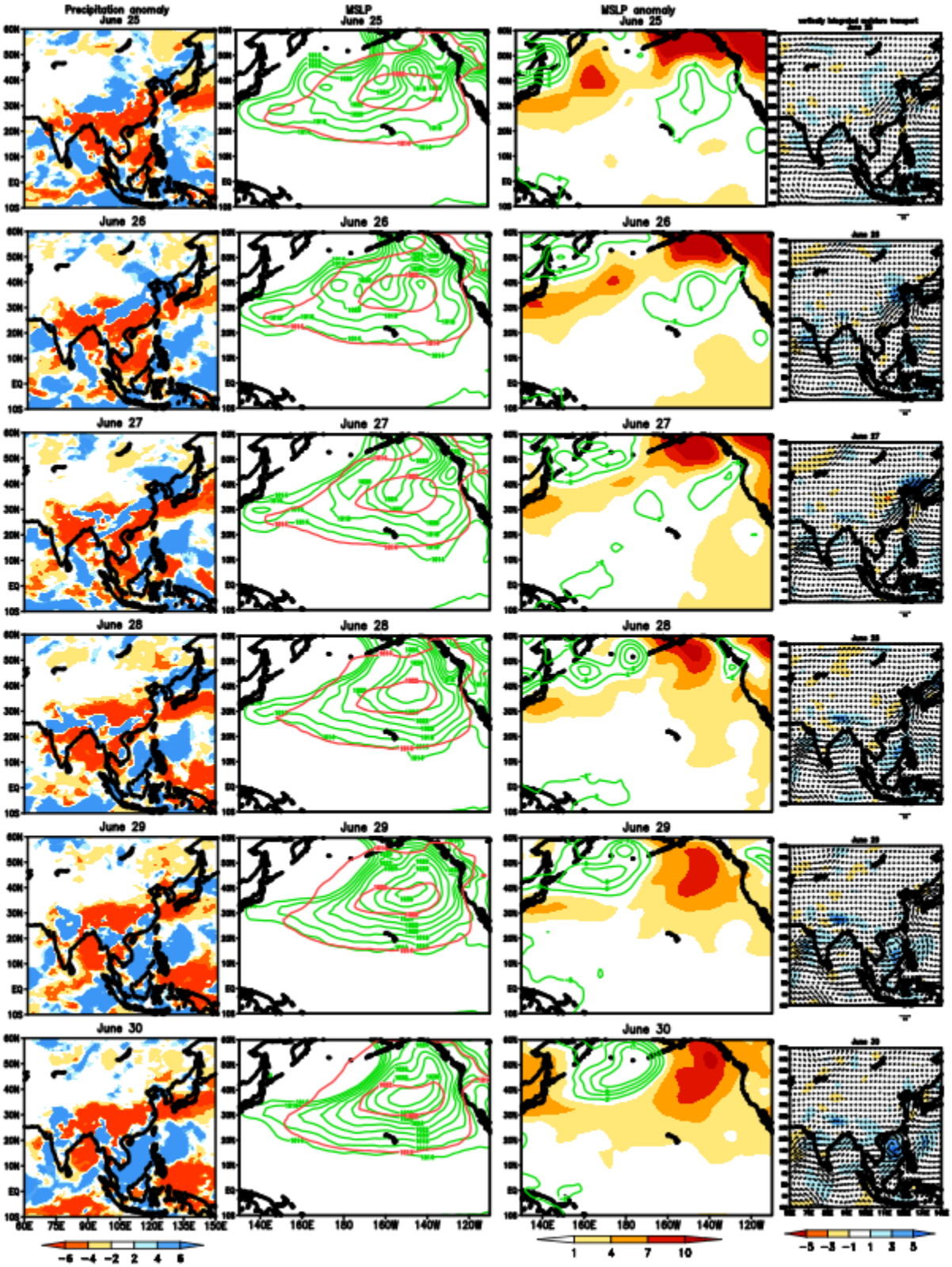

Figure 1. Spatial plot of daily precipitation anomaly (1st column), MSLP (green contours) overlaid by climatology (red contours of 1014hPa and 1022hPa) (2nd column), MSLP anomaly (positive: shaded, negative: green contours) (3rd column), vertically integrated moisture transport ($kg.m^{-1}.s^{-1}$: vector) overlaid by moisture flux convergence ($g.kg^{-1}.\ s^{-1}$ order 10^4: shading) from the surface to 300hPa (4th column), during 25-30th June 2022 from top to bottom respectively.

Amplitude-frequency characteristics of Atlantic Equatorial Mode variations from long-term observations

Mokhov I.I.[1,2], Medvedev N.N.[2]

[1]A.M. Obukhov Institute of Atmospheric Physics RAS

[2]Lomonosov Moscow State University

mokhov@ifaran.ru

In the Atlantic basin, the Atlantic Equatorial Mode (AEM) is manifested as an analogue of ENSO, which is formed in the Pacific basin [1–4]. We present here results of the analysis of the amplitude-frequency characteristics of the AEM variability detected by variations in the ocean surface temperature in the Atlantic 3 region (20W-0, 3S-3N) [1] (see also [2, 3]). The analysis used monthly means of the AEM index from January 1870 to December 2022 (https://www.metoffice.gov.uk/hadobs/hadisst/data/HadISST_sst.nc.gz).

Wavelet analysis [5] was used to describe the features of AEM variations. Changes in the characteristic periods (P) and amplitudes (A) of the AEM were also estimated using the method proposed in [6] (see also [7,8]). In particular, the AEM characteristic periods and amplitudes were estimated at different moving averages of the data (I_s) and for different moving time intervals (I_0).

Figure 1 shows local and integral wavelet spectra for AEM index variations in 1870-2022. There are three ranges of intradecadal and interdecadal AEM variations. On the integral spectrum, the most significant variations of the AEM index are distinguished with periods ranging from 2 to 7 years and with a maximum of about 12-13 years. There are also statistically less significant variations with a maximum around 25 years.

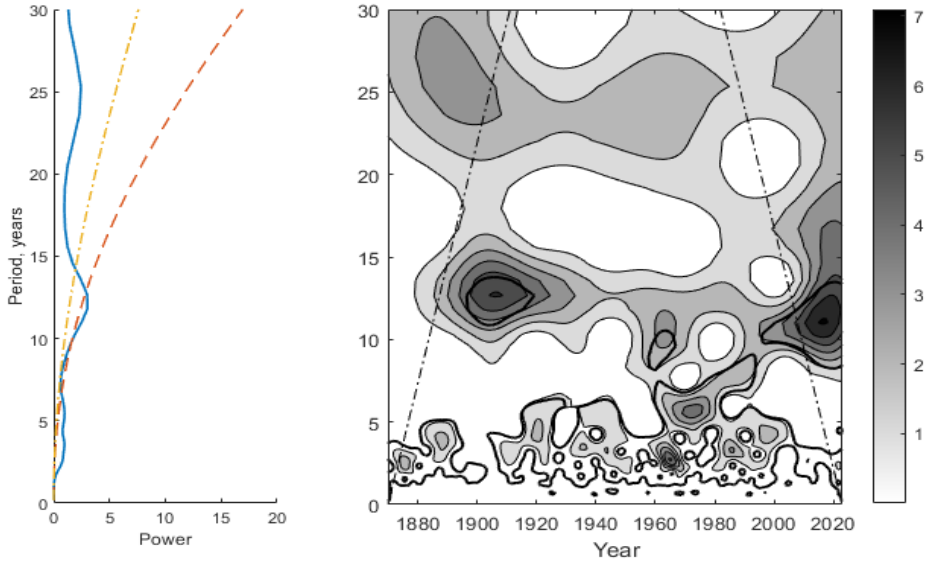

Fig. 1. Integral (left) and local (right) wavelet spectra for AEM index by the data for 1870-2022. In the integral spectrum, the dashed lines show the 95% quantile of power for a red noise model and the dotted and dashed lines indicate its mean value. The dotted and dashed lines in local spectrum separate regions of edge effects, and the thick lines bound regions where the signal power is greater than expected for a “stationary red noise model” at the significance level $p = 0.05$.

Local spectral features (Fig. 1), along with three ranges of AEM variations noted in the integral spectrum, reveal significant variations with periods from 2 to 10 years in the second half of the 20th century. Also, since the beginning of the 21st century an increase in decadal and longer-term AEM variations is revealed.

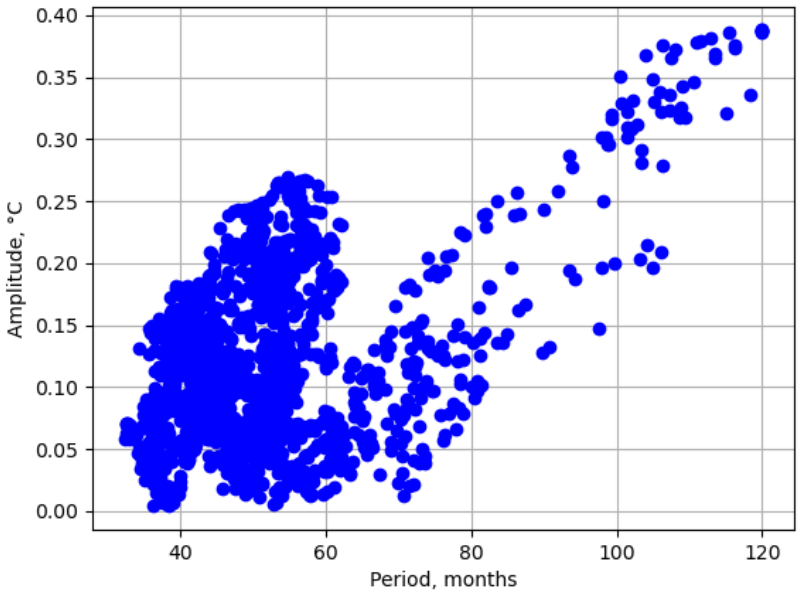

Fig. 2. Dependence of amplitudes on periods of the AEM index variations by the data for 1870–2022 at I_s = 24 months and I_0 = 120 months.

According to Fig. 2, two branches of the A-P dependence for AEM appear - for variations with *P* from 3 to 5 years and for variations with *P* more than 5 years. Different A-P dependences in Fig. 2 correspond to two ranges of periods of the AEM intradecadal and decadal variations noted in Fig. 1.

References

1. Zebiak S.E. Air-sea interaction in the equatorial Atlantic region. *J. Clim.*, 1993, **6**, 1567–1586.
2. Keenlyside N.S., Latif M. Understanding equatorial Atlantic interannual variability. *J. Clim.*, 2007, **20**, 131-142.
3. Mokhov I.I., Bezverkhny V.A., Karpenko A.A., Keenlyside N.S., Kozlenko S.S. Cross-wavelet analysis of coherence and time lags between El Nino and Atlantic equatorial mode. *Research Activities in Atmospheric and Oceanic Modelling*, J. Cote (ed.). WMO TD-No.1397, 2007, 2, 19-20.
4. Kozlenko S.S., Mokhov I.I., Smirnov D.A. Analysis of the cause and effect relationships between El Niño in the Pacific and its analog in the equatorial Atlantic. *Izv., Atmos. Oceanic Phys.*, 2009, **45** (6), 704–713.
5. Jevrejeva S., Moore J., Grinsted A. Influence of the Arctic Oscillation and El Niño-Southern Oscillation (ENSO) on ice conditions in the Baltic Sea: The wavelet approach. *J. Geophys. Res.*, 2003, **108** (D21), 4677, doi:10.1029/2003JD003417.
6. Mokhov I.I. Climate changes: Analyses of global cycles. *Ann. Geophys.* 1993, **12** (Suppl. II), C334.
7. Mokhov I.I., Medvedev N.N. Changes of the El Niño quasi-cyclic dynamics from the analysis of phase portraits. *Research Activities in Earth System Modelling*, E. Astakhova (ed.), 2021, Rep. 51, 2, 13-14.
8. Mokhov I.I., Medvedev N.N. The amplitude–frequency features of different El Nino types and their changes in recent decades. *Moscow Univ. Phys. Bull.*, 2022, **77** (3), 542–548.

Coherence of the Antarctic ice core data from the Vostok station and EPICA

Mokhov I.I.[1,2], Nyrov A.O.[2]

[1]A.M. Obukhov Institute of Atmospheric Physics RAS

[2]Lomonosov Moscow State University

mokhov@ifaran.ru

Consistency of the Antarctic ice core data for temperature and CO_2, CH_4 and dust (D) concentrations in the atmosphere from the Russian Vostok station [1] and EPICA Dome C (EDC) [2] for the past more than 400 thousand years (kyr) is estimated with the use of cross-wavelet analysis and linear regressions [3] (see also [4-7]).

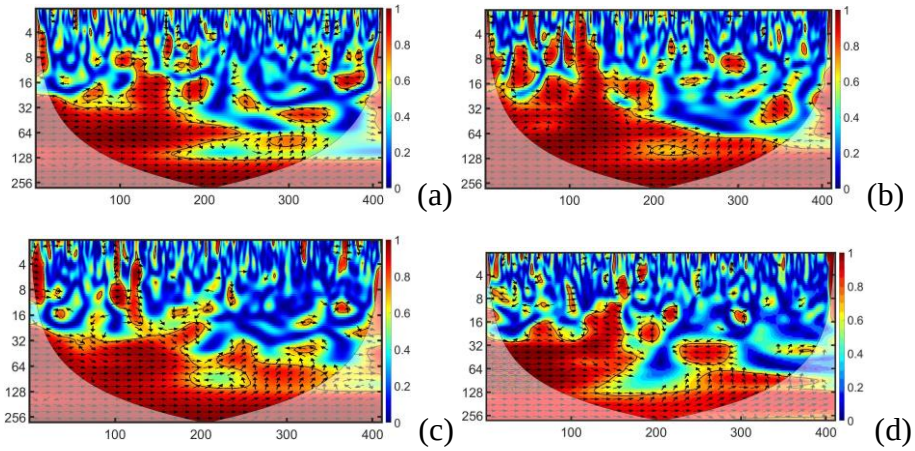

Figure 1. Coherence of variations of temperature (a), CO_2 (b), CH_4 (c) and dust (d) concentrations in the atmosphere from EDC and Vostok ice core records. Ordinates – periods in kyr before present (BP). Areas with significant coherence (95%) are highlighted, arrows characterize the phase shift (right-pointing arrow - in-phase, left-pointing arrow - antiphase). The boundaries of manifestation of edge effects are also marked.

Figure 1 shows coherence of variations of temperature T (a), q_{CO2} (b), q_{CH4} (c) and q_D (d) concentrations in the atmosphere from EDC and Vostok ice core records. The obtained results show a more significant agreement between the paleoreconstructions of EPICA and Vostok for the longest-term variations with a period of about 100 kyr or more. For shorter periods, the consistency of different data is best within the past 200 kyr.

Table 1. Coefficients of linear regressions of EPICA data (T, q_{CO2}, q_{CH4}, q_D) on corresponding Vostok data for different 100 kyr time intervals BP (I, II, III, IV and I+II+III+IV): k – regression coefficients, r – correlation coefficients.

		I+II+III+IV 0-400 kyr BP	I 0-100 kyr BP	II 100-200 kyr BP	III 200-300 kyr BP	IV 300-400 kyr BP
k (r)	T	1.32 (0.72)	1.49 (0.90)	1.73 (0.94)	0.78 (0.45)	0.79 (0.41)
	CO_2	0.83 (0.86)	0.98 (0.94)	0.93 (0.97)	0.52 (0.54)	0.74 (0.77)
	CH_4	0.73 (0.71)	0.77 (0.74)	0.76 (0.86)	0.42 (0.40)	0.54 (0.51)
	D	0.54 (0.51)	0.87 (0.79)	0.76 (0.74)	0.07 (0.06)	0.46 (0.38)

Table 1 shows coefficients of linear regressions of EPICA data (T, q_{CO2}, q_{CH4}, q_D) on corresponding Vostok data for different 100 kyr time intervals BP (I, II, III, IV and I+II+III+IV): k – regression coefficients, r – correlation coefficients. According to Table 1 the best agreement of different data is displayed for the past 200 kyr (I,II).

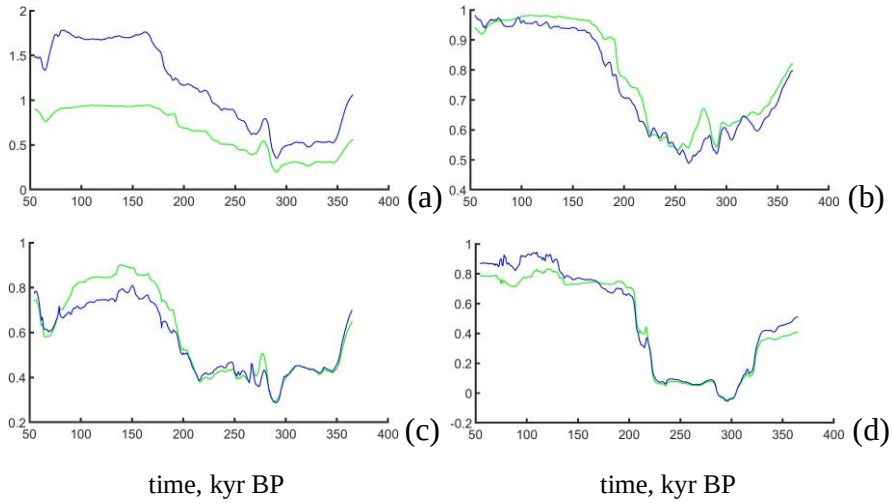

Figure 2. Coefficients of linear regressions of EPICA data on corresponding Vostok data for moving 100 kyr time intervals in dependence on time (kyr BP): (a) T, (b) q_{CO2}, (c) q_{CH4}, (d) q_D . Blue lines - coefficients of regression, green lines – coefficients of correlation.

Figure 2 shows coefficients of linear regressions of EPICA data on corresponding Vostok data for moving 100 kyr time intervals in dependence on time: (a) T, (b) q_{CO2}, (c) q_{CH4}, (d) q_D. According to Fig. 2 the best consistency of different data is exhibited within the past 200 kyr, especially for q_{CO2}.

As a whole, the results obtained show the best agreement between EPICA and Vostok data within the past 200 kyr.

References

1. Petit J.R., Jouzel J., Raynaud D. et al., 1999: Climate and atmospheric history of the past 420000 years from the Vostok ice core, Antarctica. *Nature*, 399, 429-436.
2. EPICA community members, 2004: Eight glacial cycles from an Antarctic ice core. *Nature*, 429, 623-628.
3. Grinsted A., Moore J.C., Jevrejeva S., 2004: Application of the cross wavelet transform and wavelet coherence to geophysical time series. *Nonlinear Processes in Geophysics*, 11, 561-566.
4. Mokhov I.I., Bezverkhny V.A., Karpenko A.A., 2002: Mutual dynamics of atmospheric components and climatic characteristics during last 420,000 years from Vostok ice core. *Research Activity in Atmospheric and Oceanic Modelling*. H. Ritchie (ed.). WMO/TD-No.1105, 2.17-2.18.
5. Mokhov I.I., Bezverkhny V.A., Karpenko A.A., 2005: Diagnosis of relative variations in atmospheric greenhouse gas contents and temperature from Vostok Antarctic ice core paleoreconstructions. *Izvestiya, Atmospheric and Oceanic Physics*, 41(5), 523-592.
6. Mokhov I.I., Bezverkhny V.A., Karpenko A.A., 2010: Relative changes in temperature and concentration of greenhouse gases in the atmosphere from paleoreconstructions for last 800 ka. In: *Extreme Environmental Hazards and Catastrophes. V. I. Evaluation and Ways to Reduce Negative Consequences of Extreme Environmental Phenomena*. RAS, Moscow. 312-319. (in Russian)
7. Mokhov I.I., Bezverkhny V.A., Larkina I.S., 2015: Relative variations of temperature and aerosol concentration in the atmosphere from Antarctic ice cores. *Research Activities in Atmospheric and Oceanic Modelling*. E. Astakhova (ed.). WCRP Rep. No.12/2015, 2.4–2.5.

Frequency of winter atmospheric blockings in the Northern Hemisphere in different phases of El Niño, Pacific Decadal and Atlantic Multidecadal Oscillations

Mokhov I.I.[1,2], Timazhev A.V.[1]

[1]A.M. Obukhov Institute of Atmospheric Physics RAS, Moscow
[2] Lomonosov Moscow State University
mokhov@ifaran.ru

Estimates of regional anomalies in the frequency of winter atmospheric blockings in different phases of the El Niño events, the Pacific Decadal (PDO) and Atlantic Multidecadal (AMO) Oscillations are presented using ERA-Interim reanalysis data (https://apps. ecmwf.int/datasets/data/interim-full-daily/) for the period 1979-2018. Regional features of blockings during El Niño of different types are estimated.

Atmospheric blockings were detected similarly to [1-4] using the approach proposed in [5] (see also [6]).

Positive (> 0.1 ºC), negative (< -0.1 ºC), neutral phases of AMO and positive (> 0.5 ºC), negative (< -0.5 ºC), neutral phases PDO were determined for winter seasons (DJF) using data from (https://psl.noaa.gov/gcos_wgsp/). Positive, negative and neutral phases of El Niño were determined by anomalies (with a threshold of +/- 0.5 ºC) of Niño3 and Niño4 indices (5-months running means) during the 6 consecutive months using data from (https://psl.noaa.gov/gcos_wgsp/).

Figure 1 shows winter blocking frequency in the mid-latitudes of the Northern Hemisphere for years beginning in the different phases of El Niño using the Niño3 and Niño4 indices, with different phases of wintertime AMO and PDO phases for the period 1979-2018. The obtained results show significant regional anomalies of the frequency of winter atmospheric blockings in the Northern Hemisphere in different phases of El Niño phenomena, PDO and AMO according to data for recent decades. Remarkable differences of blocking frequency were noted with the use of different El Niño indices.

During the neutral phase of El Niño, the frequency of winter blockings in the Northern Hemisphere is generally higher in the positive PDO phase than in the negative one, and relative to the mean values for the entire analyzed period (1979-2018). In the negative PDO phase over extended areas, reduced blocking frequency values were noted, in particular, over the Atlantic and Pacific oceans and over Asian regions. Also, the frequency of winter blockings in the negative AMO phase is greater than in the negative phase and relative to the mean values for the entire analyzed period for many regions, in particular, over the Pacific Ocean and most of Eurasia.

In the warm phase of El Niño over many areas, a reduced frequency of winter blockings was noted during positive PDO phase. Extreme patterns of frequency for winter blockings during El Niño, characterized by the Niño4 index, were noted in the negative PDO phase. The maximum blocking frequency values were noted over the Pacific Ocean and European regions, and the minimum values were noted over the Asian and North American regions and the Atlantic Ocean. In the warm El Niño phase, the blocking frequency values were estimated to be larger in the positive AMO phase than in the negative one over the Pacific and Atlantic Oceans and North American regions and smaller over the European regions.

In the La Niña phases, large variations in the frequency of winter blockings depending on the PDO and AMO phases were noted, in particular, over the Ural Mountains and adjacent regions.

It should be noted the low frequency of some combinations of the El Niño and La Niña phases with the PDO and AMO phases. In particular, for the analyzed period, not a single combination of the canonical El Niño phase (characterized by the Niño3 index) and the negative PDO phase was identified.

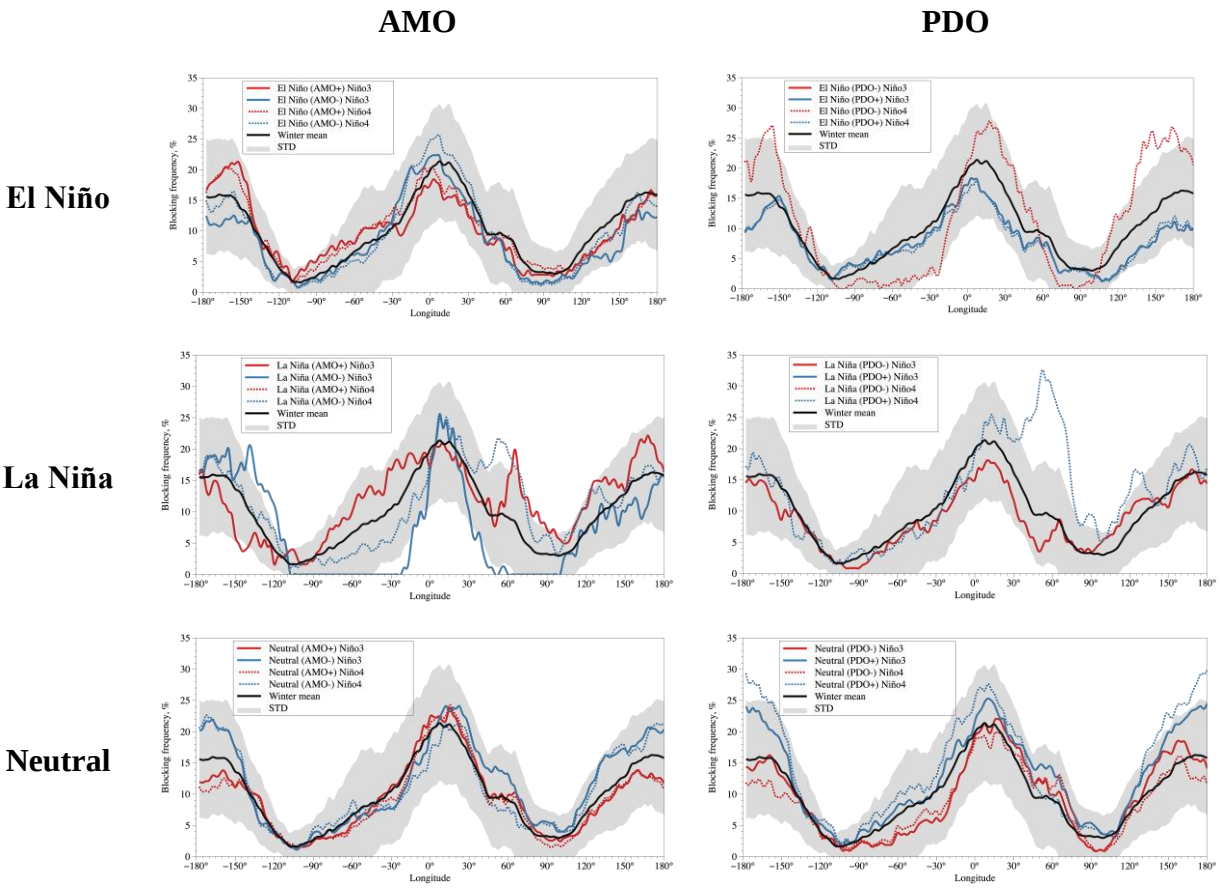

Figure 1. Winter blocking frequency in the mid-latitudes of the Northern Hemisphere for years beginning in the different phases of El Niño using the Nino3 and Nino4 indices, with different phases of wintertime AMO and PDO phases against the background of means with shaded range of standard deviations (STD) for the period 1979-2018.

References

[1] Wiedenmann J.M., Lupo A.R., Mokhov I.I., Tikhonova E.V. The climatology of blocking anticyclones for the Northern and Southern Hemispheres: Block intensity as a diagnostic. *J. Climate*, 2002, **15**, 3459-3473.

[2] Mokhov I.I., Timazhev A.V., Lupo A.R. Changes in atmospheric blocking characteristics within Euro-Atlantic region and Northern Hemisphere as a whole in the 21st century from model simulations using RCP anthropogenic scenarios. *Glob. Planet. Change*, 2014, **122**, 265-270.

[3] Mokhov I.I., Timazhev A.V. Atmospheric blocking and changes in its frequency in the 21st century calculated with the ensemble of climate models. *Russ. Meteorol. Hydrol*., 2019, **44** (6), 369–377.

[4] Lupo A.R., Jensen A.D., Mokhov I.I., Timazhev A., Eichler T., Efe B. Changes in global blocking character during recent decades. *Atmosphere*, 2019, **10** (2), 92. https://doi.org/10.3390/atmos10020092

[5] Lejenäs H. and Øakland H. Characteristics of northern hemisphere blocking as determined from long time series of observational data. *Tellus*, 1983, **35A,** 350–362.

[6] Tibaldi S., Molteni F. On the operational predictability of blocking. *Tellus A*, 1990, **42** (3), 343-365.

Low-level Cloud trends and its relationship with Indian Summer Monsoon

Amita Prabhu[1,*], Sujata K. Mandke[1] and G. Pandithurai[1]
[1] Indian Institute of Tropical Meteorology, Ministry of Earth Sciences, India
*amitaprabhu@tropmet.res.in

1. Introduction

India Summer Monsoon Rainfall is one of the prime phenomena having a profound impact on the socio-economic growth of the country (Gadgil, 2003). Clouds typically cover almost two third of the global surface and are responsible for rainfall. Clouds are generally produced over the warm and moist regions assisted by atmospheric motions, wherein its vertical structure is particularly indicative of the motions producing the clouds, in addition to most of the cloud properties that are generally produced by the same event (Rossow and Schiffer, 1999). Implications of external remote forces on the distribution of clouds and summer monsoon rainfall have been studied earlier employing International Satellite Cloud Climatology Project (ISCCP) dataset (Prabhu et al., 2018). This study elucidates trends in Low-level clouds and its relationship with summer monsoon rainfall over India.

2. Data and methodology

Gridded Rainfall data (0.25° x 0.25°) developed by India Meteorological Department (IMD) (Pai et al., 2014), from a finely distributed network of 6955 rain gauges spread across the entire Indian landmass is utilised for the period 1984-2009. ISCCP D2 data, has been employed for the period 1984-2009 for observing the distribution of large-scale low-level cloud features. As per ISCCP cloud classification (Rossow and Schiffer, 1999), low-level clouds are estimated from the Cloud Top Pressure (CTP), which is in the range of 1000 to 680 hPa, while the Cloud Optical Thickness (COT) is in the range of 0–379. The cloud amount estimation is done by evaluating each pixel of 5 km across for a particular level by counting the number of pixels that are marked as cloudy and dividing by the total number of pixels in a region of about 280 km across and this dataset is available online (http://isccp.giss.nasa.gov/products/products.html). Further, trend for the inter-annual time series of low-level cloud amount index constructed by averaging over the Indian region [8°-38°N, 68°-98°E] during June through September (JJAS) based on the period 1984-2009 is examined by using a standard *F* test statistic that assesses the null hypothesis of zero slopes (Kendall and Stuart, 1979). Furthermore, correlation coefficients (CC) are computed to determine the spatial relationship between the low-level cloud amount index over the Indian region and rainfall at each grid during JJAS based on the above period, and checked for its significance at 95% confidence level, employing student's T test statistic (Kendall and Stuart, 1979). Both the time series are detrended and standardised prior to calculation of CC.

3. Results

Following inferences are drawn considering the connection between ISCCP's low-level clouds and summer monsoon rainfall over India as shown in Figure 1:

1) A significant increasing trend in standardised Low-level cloud amount index is observed over the period 1984-2009.

2) Spatial plot of trend for Low-level cloud amount during JJAS based on the period 1984-2009 depicts significant decreasing trend over the western parts of India and significant increasing trend over the southeast peninsular India along with adjoining regions of southwest Bay of Bengal.

3) CC of low-level cloud amount averaged over the Indian domain with that of rainfall at each grid point over India during JJAS season depicts larger spread of negative relationship between the two, implying deficit summer monsoon rainfall for excessive Low-level clouds.

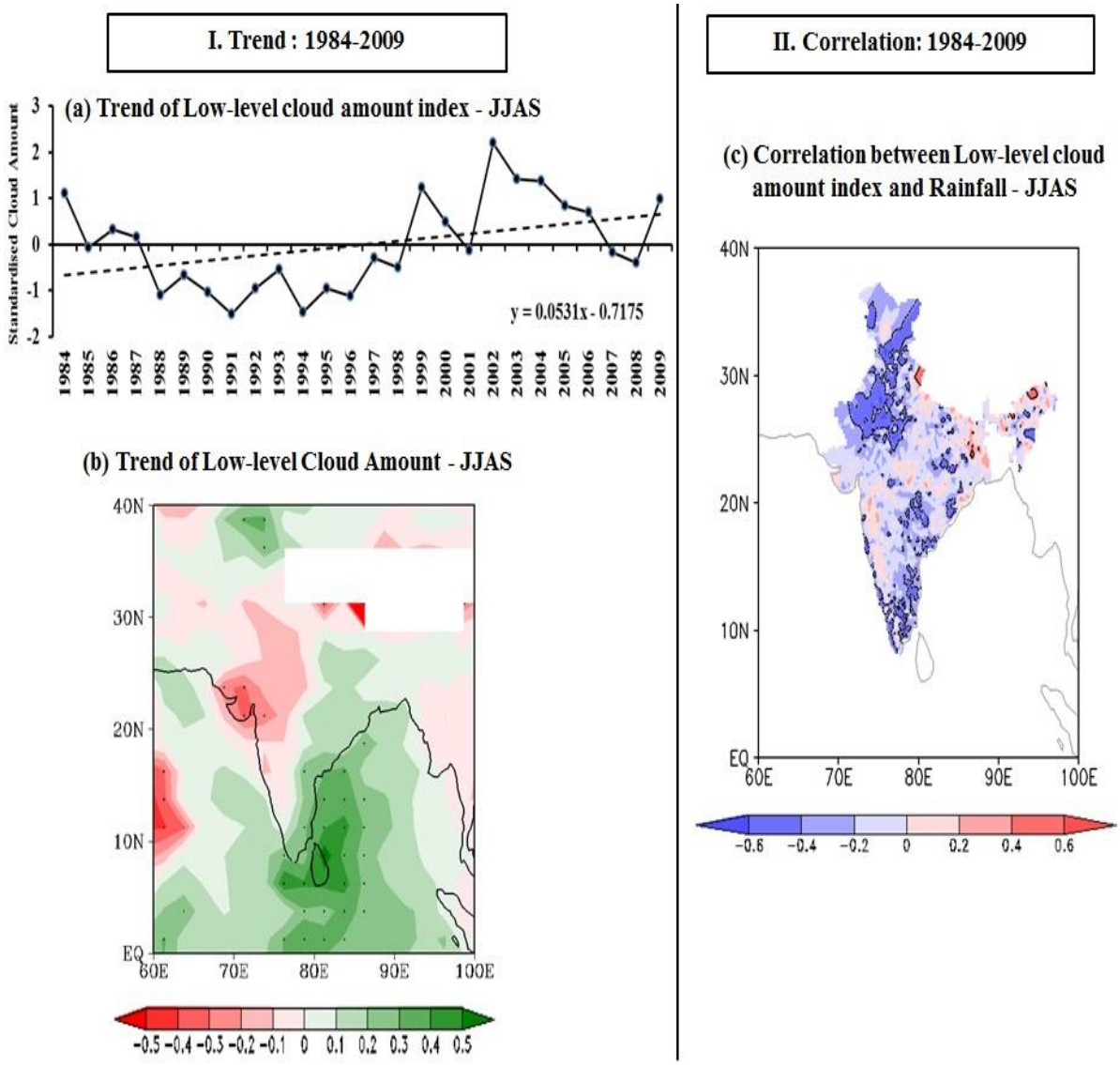

Figure 1. Set I. (a) Inter-annual variability of Low-level cloud amount index during JJAS averaged over the Indian region [8°-38°N, 68°-98°E] over the period 1984-2009, wherein dotted line indicate its trend; (b) Spatial plot of trend of Low-level cloud amount during JJAS based on the period 1984-2009; Set II. (c) Spatial Correlation (shaded) of Low-level cloud amount index with that of rainfall at each grid point over the Indian region during JJAS based on the period 1984-2009, whereas contours in black indicate significance of correlations at 95% confidence level.

References

Gadgil S. 2003. The Indian monsoon and its variability. Annu Rev Earth Planet Sci 31:429–467.

Kendall MG, Stuart A. 1979. The advanced theory of statistics, volume 2: inference and relationship, griffin, 4th edn, Hodder Arnold publisher, London, pp. 758 (ISBN:0852642555)

Pai DS, Sridhar L, Rajeevan M, Sreejith OP, Satbhai NS, Mukhopadhyay B. 2014. Development of a new high spatial resolution (0.25 × 0.25 degree) long period (1901–2010) daily gridded rainfall data set over India and its comparison with existing data sets over the region. Mausam. 65(1): 1–18

Prabhu A, Pandithurai G. 2018. ISCCP observed large-scale cloud features over the Indo-Pacific, Southern Annular Mode and Indian summer monsoon. Polar Sci. 18: 167-175

Rossow WB, Schiffer RA. 1999. Advances in understanding clouds from ISCCP. Bull. Am. Meteorol. Soc. 80: 2261–2288.

Evolution of wind patterns over the tropical summer monsoon region influenced by wintertime southern annular mode in the recent decades

Amita Prabhu[1,*] and G. Pandithurai[1]
1 Indian Institute of Tropical Meteorology, Ministry of Earth Sciences, India
*amitaprabhu@tropmet.res.in

1. Introduction

Southern Annular Mode (SAM) (Limpasuvan and Hartmann, 1999), which is also referred to as high-latitude modes (Rogers and van Loon, 1982), is principle mode of variability in wind fields characterized by north-south vacillations over the southern polar region and the mid-latitudes. Association between SAM and the India summer monsoon rainfall (ISMR) has been examined in the recent decades 1983–2013, which indicate that February–March SAM is significantly related with the subsequent ISMR. A positive (negative) SAM during February–March is favorable (unfavorable) for the ensuing summer monsoon rainfall over the Indian sub-continent (Prabhu, et al. 2016). Further, linkages between SAM and the Korean Summer Monsoon Rainfall (JJA: KMR) based on the same data period demonstrates that the May-June SAM is positively connected with the subsequent KMR (Prabhu et al. 2017). In both these Asian summer monsoon subsystems, the sub-polar signal of SAM is relayed through the central Pacific Ocean. Considering the influence of SAM variability during late winter/early spring on the Asian summer monsoon subsystems, the evolution of wind patterns is assessed over the tropical domain (40°S to 40°N) across all the longitudes to understand its impact on the unexplored domain of African Summer monsoon along with South Asia (in particular India) and East Asia (in particular South Korea-Japan peninsula) summer monsoon regions.

2. Data

Monthly mean sea level pressure (MSLP) and winds (m/s) at 850 hPa have been obtained from National Center for Environmental Prediction (NCEP) and the National Center for Atmospheric Research (NCAR) reanalysis (Kalnay et al. 1996). Following Nan and Li (2003), SAM Index (SAMI) has been generated (SAMI = MSLP40 – MSLP70), wherein the parameters MSLP40 and MSLP70 represent normalized zonal MSLP values at 40°S and 70°S respectively. To evaluate the wind patterns generated from extreme episodes of wintertime (averaged over the months of January and February) SAM Index (SAMI), extreme positive and negative years of SAMI are identified. The years with standardized value of SAMI greater than +1 are referred as positive SAM years and less than -1 as negative SAM years. Further, simple statistical technique of composite analysis has been utilised.

3. Results

From the evolution of wind anomalies (Figure 1) from January through September at 850 hPa atmospheric low-level vector winds, following inferences have been drawn:

1) A weakened low-level (at 850 hPa) South Asian monsoon flow is evident during the negative extremes of SAM building up from May-June up to August-September, which inhibits monsoon circulation causing weakened rainfall over the Indian region, in agreement with the results shown earlier using February-March SAMI (Prabhu et al. 2016).
2) A weakened north Pacific sub-tropical high is also observed building up from May-June through July-August that constrains supply of moisture flux to East Asia, weakening its summer monsoon rainfall, in concord with study carried out earlier using May-June SAMI (Prabhu et al. 2017).
3) Further, over the African continent, the moisture laden low-level winds (May-June through August-September) from the Atlantic Ocean basin towards the western coast of Africa, which strengthens the rainfall particularly for the Sahel region, appears to have reversed, weakening its rainfall over this domain.

In summary, the high latitude SAM is significant to understand the dynamics of summer monsoon over the tropical belt. However, this is a preliminary study to understand the wintertime effect on the evolution of low-level wind patterns over the tropics encompassing important summer monsoon systems that requires thorough investigation.

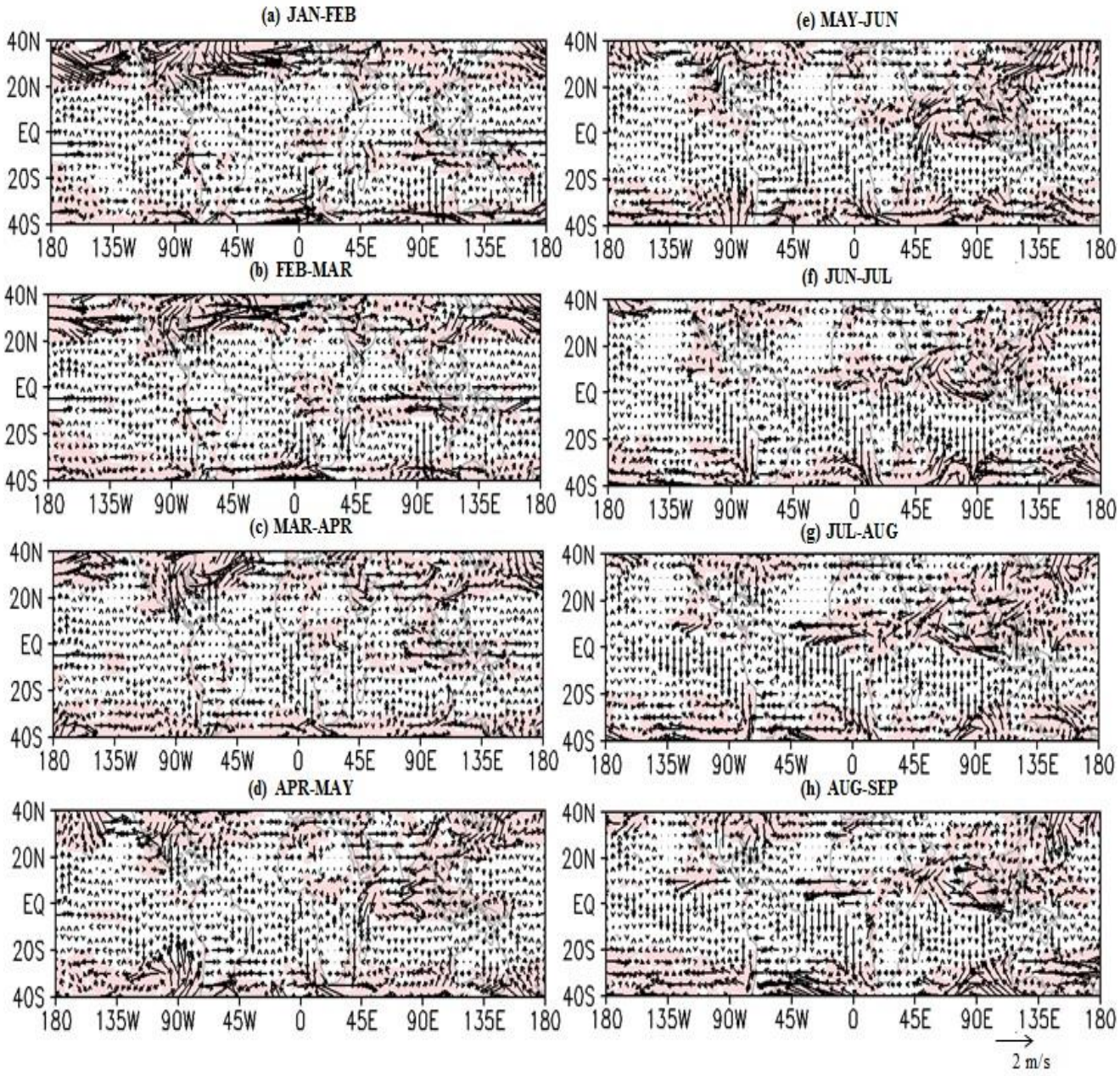

Figure 1. Winds at 850 hPa constructed from composites of 10 (Negative - Positive) modes of January-February SAMI extremes during the period 1983-2017. Significant differences at 95% confidence level in wind anomalies are shaded.

References

Kalnay E. et al. 1996. The NCEP/NCAR 40-year reanalysis project. Bull. Am. Meteorol. Soc. 77:437–471

Limpasuvan V, Hartmann DL. 1999. Eddies and the annular modes of climate variability. Geophys. Res. Lett. 26: 3133–3136.

Nan S, Li J. 2003. The relationship between summer precipitation in the Yangtze River valley and the previous Southern Hemisphere Annular Mode. Geophys Res Lett 30(24): 2266

Prabhu A, Kripalani RH, Preethi B, Pandithurai G. 2016. Potential role of the February-March Southern Annular Mode on the Indian summer monsoon rainfall: a new perspective. Clim. Dyn. 47: 1161-1179.

Prabhu A, Kripalani RH, OH J, Preethi B. 2017. Can the Southern Annular Mode influence the Korean Summer Monsoon Rainfall? Asia-Pacific J. Atmos. Sci. 53: 217-228.

Rogers JC, van Loon H. 1982. Spatial variability of sea level pressure and 500mb height anomalies over the Southern Hemisphere. Mon. Wea. Rev. 110:1375–1392.

IMDAA high resolution regional reanalysis for the Indian monsoon region

S. Indira Rani and John P. George
National Centre for Medium Range Weather Forecasting (NCMRWF),
Ministry of Earth Sciences (MoES),
A-50, Institutional Area, Sector-62, Noida-201301, U.P., India
indirarani.s@gov.in, indira@ncmrwf.gov.in, john@ncmrwf.gov.in

"Indian Monsoon Data Assimilation and Analysis (IMDAA)" is a high resolution satellite-era regional reanalysis produced by National Centre for Medium Range Weather Forecasting (NCMRWF) in collaboration with the Met Office, UK and India Meteorological Department (IMD) under the National Monsoon Mission (NMM) Project of Ministry of Earth Sciences, Government of India. IMDAA was conceived as a 40 years reanalysis from 1979 to 2018, and later the same was extended to 2020. IMDAA is the highest resolution reanalysis, 12 km, currently available over the Indian monsoon region. This reanalysis was produced using the state-of-the-art data assimilation and modeling system (domain is given in Figure-1 and details are given in Table 1).

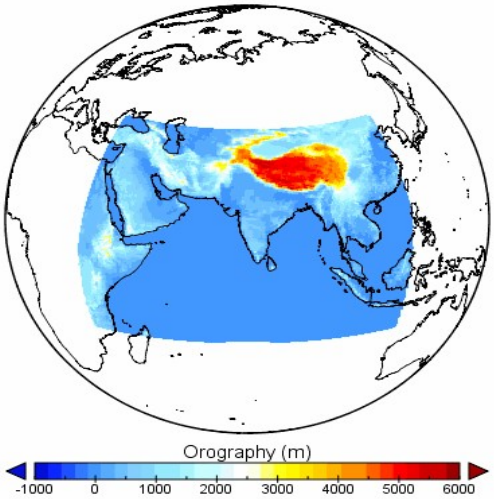

Figure 1: IMDAA domain with overlaid orography in meters

Table 1: IMDAA configurations

Period	1979-2018, extended to 2020 (42 years)
Domain	30°E- 120˚E, 15˚S to 45˚N
Lateral Boundary Conditions (LBC)	ERA-Interim
Data Assimilation method	4D-Var (Atmosphere) Extended Kalman Filter (EKF) method for Soil Moisture
Atmospheric Model	Unified Model
Horizontal Resolution	~12km (~0.11˚)
Vertical Levels	63 levels (~ up to 40 km)
Observation Sources	ECMWF, NCMRWF, UK Met Office, IMD
Surface	Soil Moisture Analysis 4 soil levels of soil covering first 3 meters Sea Surface Temperature: HadSST2, OSTIA analysis

IMDAA used ECMWF observational dataset archived for reanalysis. Additional observations from the IMD/NCMRWF archives, which are not available in the ECMWF datasets including Indian satellite observations, were also used in the IMDAA. The lateral boundary condition for IMDAA was taken from ERA-Interim. IMDAA used Variational Bias Correction (VarBC) for the satellite radiance assimilation.

Description of IMDAA regional reanalysis, including historical data restoration, quality control of various observations, data assimilation and modeling systems, comparison of IMDAA products with ECMWF Reanalysis (ERA-5) and the characteristics of Indian south-west and north-east monsoon features are available in *Rani et al., (2021)*. Various validation and verification of IMDAA datasets are available in *Rani et al., (2020), Vishal and Rani (2022)and Ashrit et al., (2020)*. An inter comparison of various reanalysis over the Indian region shows that IMDAA better captures the heavy precipitation compared to the global reanalysis (*Singh et al., 2021*). The Outgoing Longwave Radiation (OLR) is a precursor to the Indian southwest monsoon onset and propagation. The IMDAA derived OLR has a good consensus with the satellite derived OLR over the same region. Figure 2 shows the mean daily OLR from Kalpana satellite (0.25°×0.25°) and IMDAA (0.12°×0.12°) during the Indian monsoon season, June to September (JJAS) from 2004 to 2017.

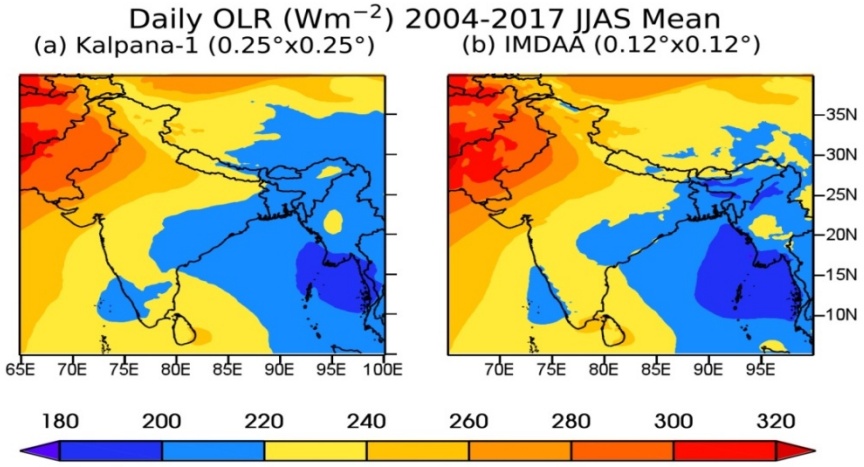

Figure 2: Comparison of mean daily OLR (a) Kalpana-1 satellite and (b) IMDAA reanalysis during June-July-August-September (JJAS) for the period 2004 to 2017.

The IMDAA regional reanalysis products are disseminated to the international researchers through the NCMRWF reanalysis portal, https://rds.ncmrwf.gov.in/. Many of the IMDAA products at 12 km spatial resolution are available at hourly intervals and the others at 3 hourly intervals. Details of the products are available at the reanalysis portal. There are approximately 2250 registered users for the IMDAA dataset till now. As per the request from the users, as continuity, NCMRWF started disseminating IMDAA-Like products from NCMRWF Unified Model (NCUM) analysis over the IMDAA domain through the reanalysis portal beyond December 2020.

References

Jisha K. Vishal, and S. Indira Rani Location-specific verification of near-surface air temperature from IMDAA regional reanalysis. *J Earth Syst Sci* , 131, 179 (2022). https://doi.org/10.1007/s12040-022-01935-9

Raghavendra Ashrit, S. Indira Rani, Sushant Kumar, S. Karunasagar, T. Arulalan, Timmy Francis, Ashish Routray, S. I. Laskar, Sana Mahmood, Peter Jermey, Adam Maycock, Richard Renshaw, John P. George, and E. N. Rajagopal (2020**),** "IMDAA Regional Reanalysis: Performance Evaluation During Indian Summer Monsoon Season"**,** *JGR Atmospheres*, Vol.125, Issue2, AGU Publications.doi:10.1029/2019JD030973.

S. Indira Rani, Arulalan T., John P. George, E. N. Rajagopal, Richard Renshaw, Adam Maycock, Dale Barker and M. Rajeevan, 2021: IMDAA: High Resolution Satellite-era Reanalysis for the Indian Monsoon Region, *Journal of Climate*, https://doi.org/10.1175/JCLI-D-20-0412.1

S. Indira Rani, John P. George, T. Arulalan, Sumit Kumar, M. Das Gupta, E.N. Rajagopal and Richard Renshaw (2020), "Evaluation of High Resolution IMDAA Regional Reanalysis Precipitation over India during Summer Monsoon Season", *CLIVAR Exchanges - Special Issue: India's Monsoon Mission*, No.79, Pages 31-33, November 2020 DOI: https://doi.org/10.36071/clivar.79.2020.

Tarkeshwar Singh, Upal Saha , V. S. Prasad and Munmun Das Gupta, 2021: Assessment of newly-developed high resolution reanalyses (IMDAA, NGFS and ERA5) against rainfall observations for Indian region. *Atmospheric Research*, DOI: https://doi.org/10.1016/j.atmosres.2021.105679

Representation of moist processes in NCUM operational forecasts during boreal summer monsoon over India

Mohan T. S*., Raghavendra Ashrit, K. Niranjan Kumar, A Jaya Kumar, Saji Mohandas and V. S. Prasad

National Centre for Medium-Range Weather Forecasting, Ministry of Earth Sciences, India

**mohans.thota@gov.in, mohant@ncmrwf.gov.in*

1. Introduction

Realistic simulation of the mean state of monsoon and its variability at various space and time scales either in climate models (Annamalai et al 2007) and/or in operational numerical weather prediction (NWP) systems is a major concern, due to the systematic errors and biases in model outputs, which pose a large burden for NWP models (Keane et al 2019). In general, these model biases originate from the discrepancies in the parameterization schemes of the physical processes; as a result, climate and weather forecasting communities rely on applying process-oriented diagnostics (PODs) (Maloney et al., 2019). The primary objective of this study is to assess the National Centre for medium-range weather Forecasting Unified Model (NCUM) global forecast (12km horizontal resolution) system's ability in representing PODs associated with enhanced (active) and suppressed (break) phases of the monsoon.

2. Data and Methodology:

In this work, we analysed the daily operational NCUM global forecasts during the 8 monsoon seasons (2015-2022, June through September). To examine the linkage between small-scale convection and its associated macro-scale circulation patterns, we have applied *moist static energy (MSE)* budget. It is regarded as POD that combines the physical processes influencing the moisture and temperature (Su and Neelin, 2002, Maloney et al 2009). The column-integrated moist static budget is given by equation. $\frac{\partial h}{\partial t} = -\omega\frac{\partial h}{\partial p} - V.\nabla h + LH + SH + F_{net}$

$$MSE, h = c_pT + gz + Lq$$

where T is temperature; q is specific humidity, V and ω are the wind components, LH and SH are turbulent latent and sensible heat fluxes, F_{net} is net radiative heating/cooling, and L is the latent heat of condensation (2.5×10^6 J/kg).

3. Results:

A close examination of the seasonal biases at different forecast lead times (Figure 1) depicts wet (dry) rainfall biases over the Arabian Sea (AS) and the Indian Ocean and dry biases over the Bay of Bengal (BoB) regions. Dry biases occupy a majority of the area over the northern parts of AS and the magnitude of these biases is increasing with lead time. Enhanced wet biases (~5mm/day) over the equatorial Indian Ocean (EIO) and southern AS regions influence rainfall variability over other regions of the Indian subcontinent through the interaction of equatorial waves and moist physics (Annamalai 2010). One implication of the rainfall biases is that even a relatively higher resolution model still struggles to simulate the mean monsoon state precisely and the uncertainties can further influence the associated diabatic heating (Q) and large-scale circulation.

Sensitivity of the atmospheric convection, i.e., rainfall binned w.r.t specific humidity, q vertical distribution shows mainly the boundary layer moisture (moisture below 800 hPa) is exhibiting more spread than the free troposphere and it is more apparent over land regions (Figure 2). MSE budget analysis applied to one strong individual break event (13-22 July 2019 having peak intensity on 17th July) depicts, the vertical advection of MSE is negative (positive) between 950-600 hPa (550-100 hPa) levels as expected in descending motion and MSE structure.

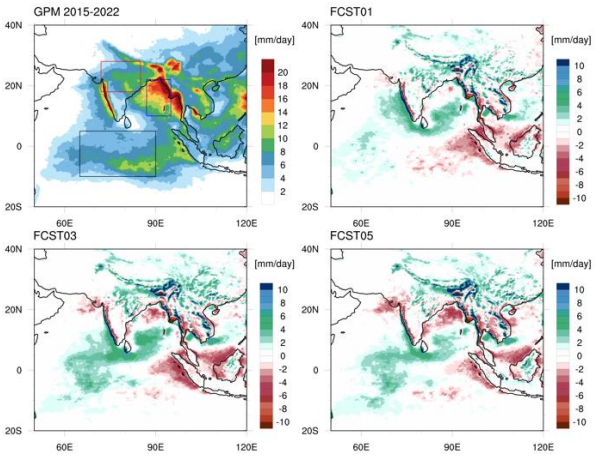

Figure 1: Mean state and forecast biases (c-d) at different lead times computed w.r.t GPM rainfall observations during monsoon.

One disparity is the presence of very high MSE seen in the model layers between the surface to 925 hPa. Horizontal advection of MSE indicates dryness prior to the peak break conditions over Central India (CI). The surface fluxes and net radiation are in phase with MSE, and the contribution of surface turbulent fluxes is relatively minimal compared to other MSE terms. Preliminary results are encouraging and indicate the advantage of using PODs as one of the verification tools for assessing model forecasts.

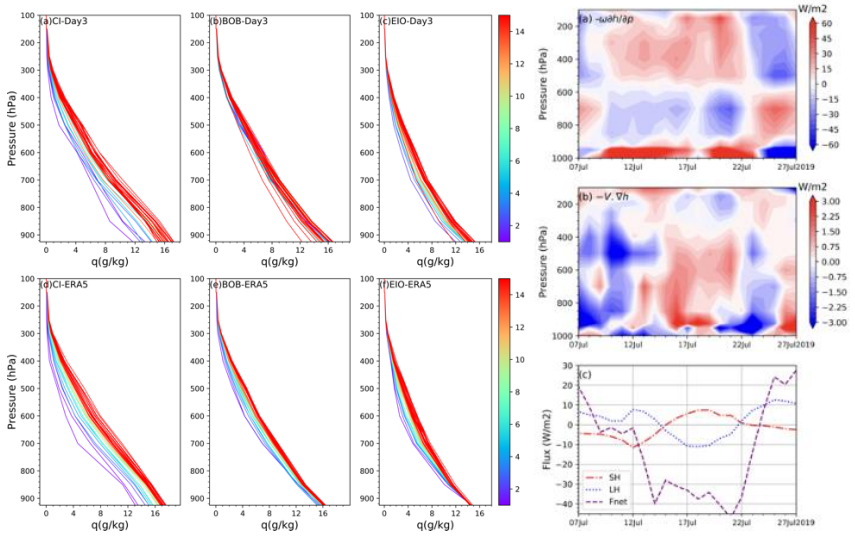

Figure 2: *Left panel:* Specific humidity averaged w.r.t.to rainfall bins over three selected regions (solid boxes in Figure 1). *Right panel:* MSE budget terms for a strong individual break event in 2019 over central India.

4. References

Rajeevan, M., S. Gadgil and J. Bhate (2010), Active and break spells of the Indian Summer monsoon. *J. Earth Syst. Sci.* **119**, 229–247.

Maloney, E. D., and et al. , 2019: Process-oriented evaluation of climate and weather forecasting models. *Bull. Amer. Meteor. Soc.*, 100, 1665–1686, https://doi.org/10.1175/BAMS-D-18-0042.1.

Su, H., and J. D.Neelin, 2002: Teleconnection mechanism for tropical Pacific descent anomalies during El Niño. J. Atmos. Sci., 59, 2694–2712

Maloney, E.D.,2009:The moist static energy budget of a composite tropical intraseasonal oscillation in a climate model. J. Climate, 22, 711–729.

Annamalai, H.,, K. Hamilton, and K. R. Sperber, 2007: South Asian summer monsoon and its relationship with ENSO in the IPCC AR4 simulations. J. Climate, 20, 1071–1092.

Keane, R. J., Williams, K. D., Stirling, A. J., Martin, G. M., Birch, C. E., & Parker, D. J.(2019). Fast biases in monsoon rainfall over southern and central India in the met office unified model. *Journal of Climate*, **32**(19), 6385– 6402. https://doi.org/10.1175/JCLI- D-18-0650.1

Study of Extreme Weather Events over India using NCMRWF Global Reanalysis

V. S. Prasad and Upal Saha

National Centre for Medium Range Weather Forecasting (NCMRWF),
Ministry of Earth Sciences (MoES),
A-50, Institutional Area, Sector-62, Noida-201301, U.P., India

vsprasad@ncmrwf.gov.in; upal@ncmrwf.gov.in

Introduction:

Using the Global Data Assimilation Forecasting System (GDAFS), the National Centre for Medium Range Weather Forecasting (NCMRWF) has been producing real-time medium-range weather forecasts, known as NGFS, since 1994 alike the Global Forecast System (GFS) model and the NCMRWF Unified Model (NCUM) over the Indian region. In order to improve this system, the 2011 version of the NGFS model and analysis scheme was used to produce a 20-year retrospective analysis known as the NGFS reanalysis for the years 1999 to 2018 (Prasad et al., 2011). In order to help the scientific community, NCMRWF produces NGFS, a high-resolution global atmospheric reanalysis. Notably, Prasad et al. (2017) made a considerable improvement to the NGFS model by raising its horizontal resolution to T574 (about 22 km) with 64 vertical levels. A wide variety of data sources are incorporated into the NGFS model, including conventional global data as well as satellite-based measurements such as atmospheric motion vector winds, radiance, and scatterometer ocean surface winds. Prasad et al. (2014) has elaborated a more thorough understanding of the parameterization techniques used in the NGFS model. Prasad et al. (2017) provide detailed information about the retrospective analysis and its value.

Key findings:

This NCMRWF Global Forecast System (NGFS) retrospective analysis data for 17 years was utilized to acquire insight into the frequency and features of cold wave episodes in Northwest India. There were 21 cold wave occurrences, making a totality of 202 cold nights between 2000 and 2016, five of which were particularly severe (63 cold nights). It's interesting to note that 10 of these incidents happened in La Nia years while just 6 did so in El Nino years, suggesting that both phases of the El Nino-Southern Oscillation are involved in the development of cold waves in the area. Based on the analysis, cold wave occurrences typically lasted ~ 9.6 days in northwest India. The longest episode ever was 26 days long and occurred in the year 2008, while the smallest episode ever was 6 days long and occurred in the year 2006. An interesting observation was that severe cold wave occurrences had an average length that was 4 days longer than that of typical cold wave episodes.

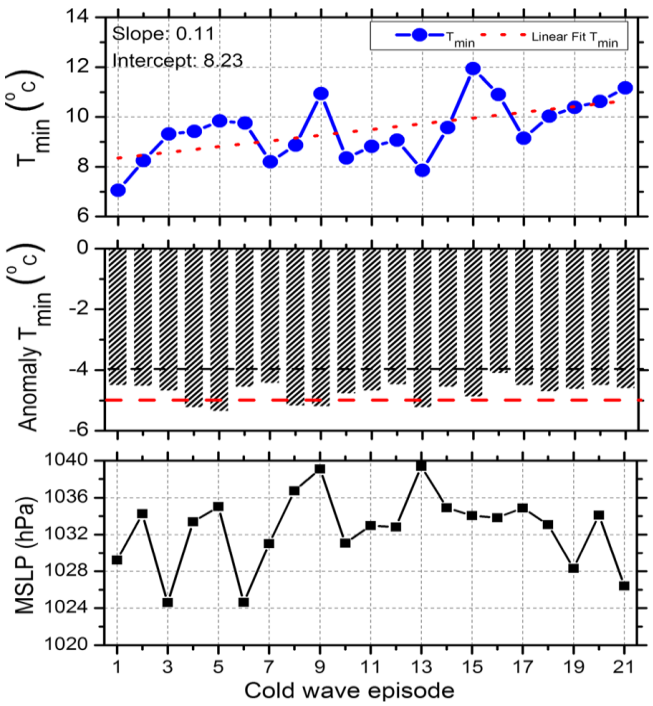

Fig. 1. *Time series of area-averaged Tmin, Tmin anomaly, and MSLP, illustrating the intra-annual variability of cold wave episodes for the study period.*

Also in 2005, the earliest cold wave onset was recorded on December 11, while the latest onset was recorded on February 16. The Siberian anticyclone and the western disturbance, which were the main causes of the cold winds in the study region, were also highlighted in the study. Anomalies in Geopotential height and temperature advection were also noted as important factors in the development of cold waves. The study also showed that there was significant intra-annual variation in the intensity of the cold waves in northwest India, with an increase of 0.11°C per cold episode. To assess the presence of intra-annual variability in cold waves (CWs) and identify any trends, an average of the minimum temperature (Tmin) over a specific area was calculated, along with its corresponding anomaly (Fig. 1). The dashed black (red) lines represent the Tmin climatological - 4°C (- 5°C). The average was taken for MSLP over (40°–60°N, and 70°–120°E) region, whereas for Tmin over the study region (Sandeep and Prasad, 2020).

Another study was performed by Singh et al. (2021) based on the comprehensive evaluation of three newly-developed high-resolution reanalysis datasets (IMDAA, NGFS, ERA5) in comparison to IMD rainfall observations during 1999-2018 over the Indian homogeneous monsoon regions.

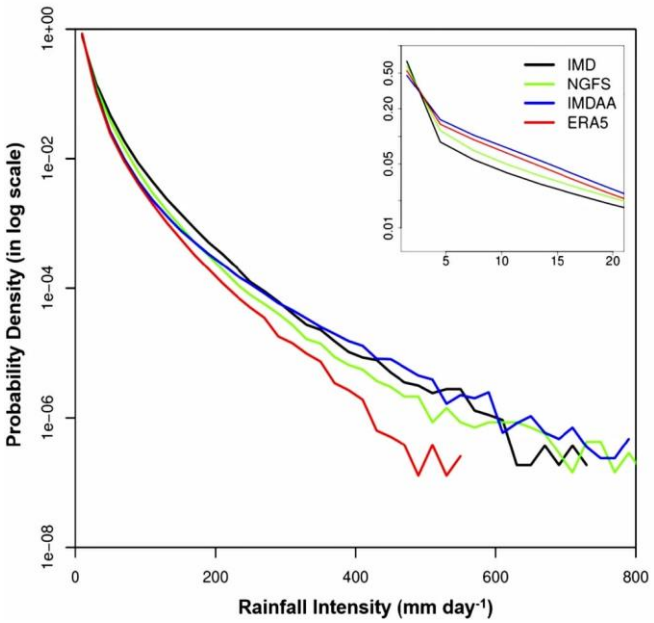

Fig. 2. *Probability Distribution for the rainfall intensity of IMD, IMDAA, NGFS and ERA5 reanalysis data respectively. Similar curve for light rain category is shown in the inset.*

The study delineates that both IMDAA and NGFS reanalysis captured the region-specific moist and desiccated trends, which is in alignment with observational trends. Moreover, both these IMDAA and NGFS reanalysis diligently captured the probability distribution of daily rainfall intensity, particularly within the range of extremes, while ERA5 reanalysis underestimated it (Fig. 2). Reasonably, NGFS performed comparatively well in capturing heavy and very heavy rainfall over the Western Ghats, surpassing IMDAA and ERA5 reanalysis. In contrast to IMDAA and NGFS reanalysis, ERA5 exhibited underestimation for all categories of extreme rainfall, as confirmed by the probability distribution curve.

References:

Prasad, V.S., Mohandas, S., Dasgupta, M., Rajagopal, E.N., Dutta, S.K., 2011. Implementation of Upgraded Global Forecasting Systems (T382L64 and T574L64) at NCMRWF. NCMR/TR/5/2011. http://www.ncmrwf.gov.in/gfs_report_final.pdf

Prasad, V.S., Mohandas, S., Dutta, S.K., Gupta, M.D., Iyengar, G.R., Rajagopal, E.N., Basu, S., 2014. Improvements in medium range weather forecasting system of India. J. Earth Sys. Sci. 123 (2), 247–258.

Prasad, V.S., Johny, C.J., Mali, P., Singh, S.K., Rajagopal, E.N., 2017. Global retrospective analysis using NGFS for the period 2000–2011. Curr. Sci. 112 (2), 370–377.

Sandeep, A. and Prasad, V.S., 2020. On the variability of cold wave episodes over Northwest India using an NGFS retrospective analysis. Pure and Appl. Geophys., 177, 1157-1166.

Singh, T., Saha, U., Prasad, V.S. and Gupta, M.D., 2021. Assessment of newly-developed high resolution reanalyses (IMDAA, NGFS and ERA5) against rainfall observations for Indian region. Atmos. Res., 259, p.105679.